

Towards a ^{229}Th nuclear clock: Understanding nucleus-electron-environment interactions

Yan-Ling Xu(徐艳玲), Hong-Yuan Zheng(郑弘远), Xi-Chen Yu(喻希辰), Yong-Hui Zhang(张永慧), Ting-Yun Shi(史庭云), and Li-Yan Tang(唐丽艳)

Citation: Chin. Phys. B, 2026, 35 (**2**): 023101. DOI: 10.1088/1674-1056/ae1f7b
http://cpb.iphy.ac.cn; http://iopscience.iop.org/cpb

What follows is a list of articles you may be interested in

Precision calculation of ^{4,6,8}He isotope shifts

Xiao-Qiu Qi(戚晓秋), Xing-Han Dong(董星汉), Fang-Fei Wu(吴芳菲), Zong-Chao Yan(严宗朝), Li-Yan Tang(唐丽艳), Zhen-Xiang Zhong(钟振祥), and Ting-Yun Shi(史庭云)

Chin. Phys. B, 2025, 34 (**11**): 113101. DOI: 10.1088/1674-1056/adf82c

Three-body physics under dissipative spin-orbit coupling

Xi Zhao(赵茜)

Chin. Phys. B, 2025, 34 (**3**): 033101. DOI: 10.1088/1674-1056/ada43e

Geometric properties of the first singlet S-wave excited state of two-electron atoms near the critical nuclear charge

Tong Chen(陈彤), Sanjiang Yang(杨三江), Wanping Zhou(周挽平), Xuesong Mei(梅雪松), and Haoxue Qiao(乔豪学)

Chin. Phys. B, 2024, 33 (**10**): 103101. DOI: 10.1088/1674-1056/ad6422

High-order Hamiltonian obtained by Foldy-Wouthuysen transformation up to the order of $m\alpha^8$

Tong Chen(陈彤), Xuesong Mei(梅雪松), Wanping Zhou(周挽平), and Haoxue Qiao(乔豪学)

Chin. Phys. B, 2023, 32 (**8**): 083101. DOI: 10.1088/1674-1056/ac9e98

Transition parameters of Li-like ions (Z=7-11) in dense plasmas

Xiang-Fu Li(李向富), Li-Ping Jia(贾利平), Hong-Bin Wang(王宏斌), and Gang Jiang(蒋刚)

Chin. Phys. B, 2021, 30 (**5**): 053102. DOI: 10.1088/1674-1056/abea80

TOPICAL REVIEW — Advances in thorium nuclear optical clocks

Towards a ^{229}Th nuclear clock: Understanding nucleus–electron–environment interactions

Yan-Ling Xu(徐艳玲)[1,2], Hong-Yuan Zheng(郑弘远)[1,2], Xi-Chen Yu(喻希辰)[1,2], Yong-Hui Zhang(张永慧)[1], Ting-Yun Shi(史庭云)[1], and Li-Yan Tang(唐丽艳)[1,†]

[1] *State Key Laboratory of Magnetic Resonance and Atomic and Molecular Physics, Wuhan Institute of Physics and Mathematics, Innovation Academy for Precision Measurement Science and Technology, Chinese Academy of Sciences, Wuhan* 430071, *China*

[2] *University of Chinese Academy of Sciences, Beijing* 100049, *China*

(Received 2 September 2025; revised manuscript received 23 October 2025; accepted manuscript online 14 November 2025)

Recent advances in atomic optical clocks based on electronic transitions have achieved frequency uncertainties at the 10^{-19} level, enabling wide applications in testing variations of physical constants, exploring dark matter signatures, and enhancing precision metrology for position, navigation, and timing systems. To pursue higher-precision optical clocks, the development of nuclear optical clocks has emerged, with the ^{229}Th system distinguished by its unique low-lying isomeric state at ~ 8.4 eV and a natural linewidth of approximately 100 μHz, promising uncertainties below 10^{-19}. The intrinsic insensitivity of nuclear transitions to external perturbations and their subatomic-scale spatial confinement provide significant advantages over electronic transitions in mitigating environmental shifts. Recent experimental breakthroughs include the excitation of the nuclear clock transition in solid-state ^{229}Th-doped crystals with spectral resolution at the kHz level. However, critical challenges persist, particularly in implementing effective laser excitation schemes (e.g., via the electronic bridge mechanism) and closed-loop quantum control in trapped ion systems. Addressing these requires comprehensive understanding of complex many-body interactions in ^{229}Th, encompassing electronic structure, nuclear deformation, hyperfine and field shift, and solid-state environmental coupling. This review synthesizes recent advancements in (i) the characterization of nuclear and atomic structures of the ^{229}Th nuclear clock, and (ii) precise evaluation and mitigation of external perturbations affecting the clock transitions. The analysis provides a solid theoretical and experimental foundation for optimizing ^{229}Th-based nuclear clock performance.

Keywords: ^{229}Th nuclear clock, electronic bridge, external field effects

PACS: 31.15.ac, 32.60.+i, 32.10.Fn, 27.90.+b

DOI: 10.1088/1674-1056/ae1f7b **CSTR:** 32038.14.CPB.ae1f7b

1. Introduction

Atomic clocks based on electronic transitions represent the state-of-the-art in time-frequency metrology, achieving fractional uncertainties at 10^{-19}.[1–3] These precise instruments play crucial roles in national timekeeping networks,[4,5] synchronization systems,[6–8] tests of fundamental constant variations,[9–11] dark matter detection experiments,[12–16] and satellite navigation systems.[17–21] The emerging nuclear optical clocks,[22–25] exploit the exceptional environmental insensitivity of nuclear transitions to achieve superb precision, with theoretical estimates indicating a potential uncertainty as low as 10^{-20}.[22]

Among all nuclides, ^{229}Th is uniquely distinguished by its nuclear isomeric state at $\omega_{\rm N} \approx 8.4$ eV (corresponding to a wavelength of ~ 148 nm),[26–29] the lowest known nuclear excitation energy. This exceptional property, combined with an ultra-narrow natural linewidth (~ 100 μHz)[30,31] and subatomic spatial confinement,[22,32–34] enables precise laser control of nuclear quantum states while minimizing environmental perturbations. Therefore, ^{229}Th has emerged as the most promising candidate for nuclear optical clocks,[35] with profound implications for fundamental physics across atomic, nuclear, and precision measurement sciences.[26,28,36–39]

The ^{229}Th nuclear clock system consists of the nucleus and the extranuclear electrons within the atom, which together interact with the external environment. As shown in Fig. 1, the nucleus and electrons perturb the energy levels of each other through Coulomb interaction and hyperfine interactions (HFI), while both are affected by external perturbations such as laser fields, thermal radiation, and electromagnetic fields. A thorough understanding of these interactions is therefore crucial for achieving precise determination of the nuclear transition energy.

Experimentally, there are two main types of ^{229}Th nuclear clocks: one based on trapped thorium ions and another utilizing doped solid-state crystals. Experimental progress has demonstrated the feasibility of ^{229}Th nuclear clock transitions via excitation and deexcitation, achieving kHz-level precision in solid-state ^{229}Th-doped crystals,[28,29] but still seven orders

†Corresponding author. E-mail: lytang@apm.ac.cn

© 2026 Chinese Physical Society and IOP Publishing Ltd. All rights, including for text and data mining, AI training, and similar technologies, are reserved.

of magnitude broader than the natural linewidth. For trapped ions implementations, however, viable effective laser excitation of nuclear transitions remains unrealized. Proposed excitation schemes, particularly the electronic bridge (EB) mechanism, where nuclear excitation is indirectly mediated by electronic transition,[40–43] face critical limitations. The excitation efficiency is influenced by precise electronic and nuclear structural data, highlighting the need for a thorough understanding of the coupling interactions between the ^{229}Th nucleus, electrons, and their surrounding environment.

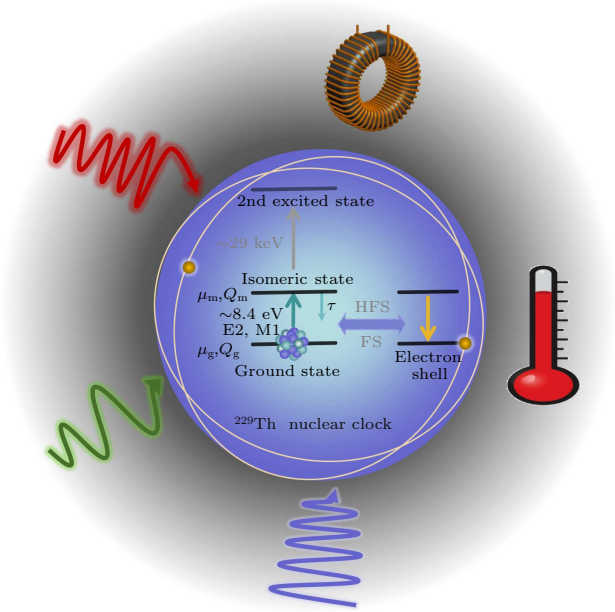


Fig. 1. The relationship among the nucleus, electrons, and external fields involves mutual perturbations of energy levels. Specifically, the nucleus and electrons perturb the energy levels of each other through field shift (FS) and hyperfine-structure (HFS) couplings, while both are further influenced by external perturbations such as laser fields, thermal radiation, and electromagnetic fields.

Theoretically, the accurate characterization of ^{229}Th faces considerable challenges. Both neutral thorium ($Z = 90$) and its ions represent complex many-body systems, where valence and core electron correlations, inner-shell excitations, nucleon interactions, and nuclear deformations all critically impact computational accuracy.[36,44–48] Compounding this complexity, current nuclear models cannot reliably predict the first excitation energy of ^{229}Th.[49] Furthermore, the scarcity of experimental data severely constrains the development of feasible EB schemes.[36,50–52]

This review systematically discusses recent advances in nucleus–electron–environment interactions, emphasizing emerging research frontiers enabled by high-precision spectroscopy of the novel ^{229}Th nuclear clock. Since the underlying physics of ^{229}Th is less well understood compared to compared to established atomic and ionic optical clocks, Section 2 summarizes the nuclear characteristics of ^{229}Th, while Section 3 details the electronic properties of various ^{229}Th ionic systems. Section 4 analyzes electron–nuclear interaction-induced frequency shifts, and Section 5 addresses various external field effects in Th-based candidates. Section 6 presents EB processes for developing trapped ^{229}Th ion clock. Finally, Section 7 outlines current challenges and future prospects in this rapidly evolving field of ^{229}Th nuclear clock.

2. Nuclear characteristics of ^{229}Th

2.1. Transition energy

Since the extremely low-energy first excited state of the thorium nucleus was first identified in the 1970s by Kroger and Reich,[53] the confirmation of its first nuclear excited energy, which is crucial for developing a nuclear clock, has been refined over decades, as shown in Table 1.

Initial measurements conducted in the 1990s at INEL Idaho reported very low energies of 1 eV and 3.5 eV, but with extremely large uncertainties of 4 eV and 1.0 eV, respectively.[54,55] These energies correspond to wavelengths of approximately 1240 nm and 354 nm, respectively. Although these results highlighted the challenge, their precision was insufficient. A pivotal measurement by LLNL in 2007 reported a significantly higher energy of 7.6(5) eV (∼163 nm),[56] substantially reducing the relative uncertainty. Subsequently, Beck *et al.* re-evaluated this measurement and corrected the energy to 7.8(5) eV,[57] which has been widely cited for many years. This established the transition in the vacuum ultraviolet (VUV) range and set the stage for more precise work. From 2019 to 2023, measurements by JAXA, LMU Munich, Heidelberg University, and KU Leuven consistently reported energies clustered around 8.1 eV to 8.3 eV (∼ 149–153 nm).[58–61] The uncertainties steadily decreased from around 0.17 eV (LMU Munich, Heidelberg University) to 0.024 eV (KU Leuven). During this period, there was a strong convergence towards the 8.3 eV region. In 2024, there was a significant improvement in precision, primarily driven by laser spectroscopy techniques on ^{229}Th doped in solid-state crystals such as CaF_2 and $LiSrAlF_6$.[26–29,62] Multiple institutions, including PTB, Okayama University, UCLA, and JILA, achieved remarkably precise energy values, all converging around 8.3557 eV. Uncertainties dropped to the milli-electronvolt (meV) and even sub-meV levels. For instance, PTB reported 8.3557(1) eV with an uncertainty of 0.1 meV. JILA reported an astonishing 8.355733552154(8) eV,[28] corresponding to a frequency measurement precision of 2 kHz. Measurements using ThF_4 in different host matrices (MgF_2, Al_2O_3) showed very slightly different energies (e.g., $8.355731(2)_{stat}(12)_{sys}$ eV, $8.355740(3)_{stat}(12)_{sys}$ eV), likely due to crystal field effects. However, these values still fell within the 8.3557 eV region with high-precision.

Table 1. Chronology of the first excitation energy and state lifetime studies for the ^{229}Th nuclear clock.

Year	Institution	ΔE (eV)	λ (nm)	ν	τ_N (s)	Method	Ref.
1976	INEL, Idaho	< 100	> 12.40	< 24.18 PHz			[53]
1990	INEL, Idaho	1(4)	1240(4959)	0.24(97) PHz			[54]
1994	INEL, Idaho	3.5(10)	354(101)	0.85(24) PHz			[55]
2007	LLNL, USA	7.6(5)	163(11)	1.84(12) PHz	5h	$^{229m}Th^{3+}$ from ^{233}U	[56]
2009	LLNL, USA	7.8(5)	159(10)	1.89(12) PHz			[57]
2019	JAXA, Japan	8.30(92)	149(17)	2.007(222) PHz		$^{229m}Th^{3+}$ from ^{233}U	[60]
2019	LMU Munich, Germany	8.28(17)	149.7(31)	2.003(41) PHz		$^{229m}Th^{3+}$ from ^{233}U	[58]
2020	Heidelberg University, Germany	8.10(17)	153.1(32)	1.958(41) PHz		^{229}Th from ^{233}U	[61]
2023	KU Leuven, Belgium	8.338(24)	148.7(4)	2.016(6) PHz	670(102)	^{229}Ac: CaF_2/MgF_2	[59]
2024	RIKEN, Japan				2020^{+866}_{-433}	$^{229m}Th^{3+}$ from ^{229}U	[65]
2024	PTB, Germany	8.355 7(1)	148.382 1(5)	2020.409(7) THz	630(15)	^{229}Th: CaF_2	[26]
2024	Okayama University, Japan	8.37(2)	148.18(42)	2.023(6) PHz	645(36)	^{229}Th: CaF_2	[62]
2024	UCLA, USA	$8.355\,733(2)_{stat}(10)_{sys}$	$148.382\,19(4)_{stat}(20)_{sys}$	$202\,040\,7.3(5)_{stat}(30)_{sys}$ GHz	$568(13)_{stat}(20)_{sys}$	^{229}Th: $LiSrAlF_6$	[27]
2024	JILA, USA	8.355 733 552 154(8)	148.382 182 8827(1)	202 040 738 433 5(2) kHz	641(4)	^{229}Th: CaF_2	[28]
2024	JILA, USA	$8.355\,731(2)_{stat}(12)_{sys}$	$148.382\,23(3)_{stat}(22)_{sys}$	$202\,040\,6.8(4)_{stat}(30)_{sys}$ GHz	$153(7)_{stat}(9)_{sys}$	$^{229}ThF_4(MgF_2)$	[63]
2024	JILA, USA	$8.355\,740(3)_{stat}(12)_{sys}$	$148.382\,06(5)_{stat}(22)_{sys}$	$202\,040\,9.1(7)_{stat}(30)_{sys}$ GHz	$150(15)_{stat}(5)_{sys}$	$^{229}ThF_4(Al_2O_3)$	[63]
2025	JILA*, USA	8.355 733 550 46(1)	148.382 182 912 8(2)	202 040 738 3.926(3) MHz		^{229}Th: CaF_2	[29]
2025	UCLA, USA	$8.355\,734\,3(6)_{stat}(12)_{sys}$	$148.382\,17(1)_{stat}(22)_{sys}$	$202\,040\,7.5(2)_{stat}(30)_{sys}$ GHz	12.3(3) μs	$^{229}ThO_2$	[64]

*Measured under $T = 229$ K condition.

The verification process for the ^{229}Th nuclear clock transition energy has evolved from highly uncertain initial estimates in the eV range to extraordinary sub-milli-eV (and even nano-eV) precision by 2024–2025. This dramatic improvement, particularly through laser spectroscopy of ^{229}Th doped in crystals like CaF_2, has firmly converged on an energy value of approximately 8.3557 eV, which corresponds to a wavelength of ~ 148.38 nm and a frequency of ~ 2.0204 PHz. This level of precision is fundamental for the development of a practical nuclear clock.

2.2. Lifetime of isomeric state

Direct nuclear structure calculations cannot predict the extremely low first excitation energy of ^{229}Th nuclei, much less their isomeric state lifetime. In experiments, this lifetime is instead inferred by detecting decay photons from the thorium isomeric state. The photon count follows the relation[63]

$$N = N_0[1 - e^{-t/\tau}], \tag{1}$$

where N_0 represents the effective number of excited ^{229}Th nuclei, and τ is the lifetime of the isomeric state.

The experimental determination of the lifetime τ_N for the ^{229}Th nuclear clock isomer has long been challenging, with no reliable values reported prior to 2023, as summarized in Table 1. Since then, however, significant progress has been made through measurements conducted in various environments.

Most experiments using ^{229}Th-doped solid-state crystals (e.g., CaF_2 and $LiSrAlF_6$) have consistently reported lifetimes on the order of hundreds of seconds. In 2023, KU Leuven reported a value of 670(102) s.[59] Subsequent measurements in 2024 further confirmed this scale: PTB reported 630(15) s,[25] Okayama University 645(36) s,[62] UCLA $568(13)_{stat}(20)_{sys}$ s,[27] and JILA 641(4) s using CaF_2.[28] In stark contrast, a recent study by UCLA in 2025, conducted with ThO_2 molecules, revealed a dramatically shorter lifetime of 12.3(3) μs via the internal conversion electron mechanism.[64] This discrepancy underscores the profound sensitivity of the isomer lifetime to its local environment, likely due to significant differences in electronic interaction strengths influencing the internal conversion decay channel — a critical consideration for nuclear clock applications.

Complementing these solid-state studies, experiments have also been performed in vacuum environments. A notable example is the RIKEN experiment, which measured a half-life of $t_{1/2} = 1400^{+600}_{-300}$ s for trapped ions under near-vacuum conditions,[65] corresponding to a state lifetime of $\tau = 2020^{+866}_{-433}$ s. The relationship between lifetimes in vacuum and crystal settings is described by $\tau_{vacuum} = n^3\tau_{crystal}$, where n is the refractive index of the crystal,[62] further highlighting the environmental dependence of the nuclear transition.

2.3. Nuclear multipole moments

In principle, nuclear multipole moments can be determined through ab-initio nuclear model calculations. Alternatively, these moments can be inferred via hyperfine interactions, where nuclear multipole moments couple to electrons. The hyperfine interaction Hamiltonian between electrons and the nucleus is given by

$$H_{HFI} = \sum_{\tau=E,M}\sum_{K\lambda}(-1)^{\lambda}\mathcal{M}^{\tau}_{K-\lambda}T^{\tau}_{K\lambda}, \tag{2}$$

where $\mathcal{M}^{\tau}_{K-\lambda}$ and $T^{\tau}_{K\lambda}$ denote the electromagnetic multipole operators of rank K for the nucleus and bound electrons, respectively. The explicit mathematical forms of these operators can be found in Refs. [66,67]. The superscript τ distinguishes between electric ($\tau = E$) and magnetic ($\tau = M$) multipole components of the interaction.

Through this interaction, the nuclear spin I and the electronic angular momentum J couple to form a total angular momentum F. The resulting wave function after the electron–nucleus coupling can be expressed as

$$|Fm_F(I\gamma J)\rangle = \sum_{m_I m_J} C(F,I,J;m_F,m_I,m_J)|Im_I\rangle|\gamma Jm_J\rangle, \quad (3)$$

where m_F denotes the magnetic quantum number of the total angular momentum F, and $C(F,I,J;m_F,m_I,m_J)$ represents the Clebsch–Gordan coefficient for angular momentum coupling. The states $|Im_I\rangle$ and $|\gamma Jm_J\rangle$ represent the nuclear and electronic wave functions, respectively, while γ encompasses additional quantum numbers.

The first-order energy correction from hyperfine interaction is given by

$$\Delta E = \frac{1}{2}AC + B\frac{\frac{3}{4}C(C+1) - I(I+1)J(J+1)}{2I(2I-1)J(2J-1)}, \quad (4)$$

where $C = F(F+1) - J(J+1) - I(I+1)$, A and B are the hyperfine structure constants. Experimentally, A and B can be determined by measuring the hyperfine splitting of electron energy levels. These constants are theoretically related to the nuclear multipole moments[66,68] through

$$A/\mu = \frac{1}{I\sqrt{J(J+1)(2J+1)}}\langle\gamma J\|T_1\|\gamma J\rangle, \quad (5)$$

$$B/Q = \sqrt{\frac{4J(2J-1)}{(J+1)(2J+1)(2J+3)}}\langle\gamma J\|T_2\|\gamma J\rangle. \quad (6)$$

Here, μ and Q represent the nuclear magnetic dipole moment and electric quadrupole moment, respectively. The operators T_K correspond to the electronic parts of the hyperfine interaction, with their explicit forms provided in Ref. [69]. Using the experimentally measured values of A and B, combined with high-accuracy theoretical calculations of the reduced matrix elements $\langle\gamma J\|T_K\|\gamma J\rangle$, the nuclear multipole moments μ and Q can be determined.

Furthermore, since the multipole moments of the nuclear ground and isomeric states satisfy Eqs. (5) and (6), and the reduced matrix element $\langle\gamma J\|T_K\|\gamma J\rangle$ of the electronic state is invariant under state transitions, the moments of one state can be derived from those of the other. This provides an alternative method for determining nuclear multipole moments.

Substituting the spins of the nuclear ground state ($I_g = 5/2$) and isomeric state ($I_m = 3/2$) into Eqs. (5) and (6), we can obtain the following relationships:

$$\mu_m = \frac{3}{5}\frac{A_m}{A_g}\mu_g, \quad (7)$$

$$Q_m = Q_g\frac{B_m}{B_g}. \quad (8)$$

Thus, once the ratio of A and B between the two states is known, the multipole moment of one state can be determined from the other. This method has been employed in previous studies.[65,68]

Table 2 comprehensively presents theoretical calculations and experimental measurements of A and B, as well as the derived μ and Q for $^{229}Th^{3+}$ and $^{229}Th^{2+}$ ions in both nuclear ground and isomeric states. It is noticed that except for the nuclear properties obtained through direct shell-model calculations in Ref. [70], the determination of all other nuclear properties relies on a combined experimental and theoretical approach to evaluate nuclear moments. For the ground state of $^{229}Th^{3+}$, the A and B have been experimentally determined for multiple electronic configurations: $5f_{5/2}$, $5f_{7/2}$, $6d_{3/2}$, $6d_{5/2}$. Campbell *et al.* measured these via optical transitions, reporting $Q_g = 3.11(16)$ eb,[71] while Zitzer *et al.* achieved a threefold reduction in uncertainties using laser spectroscopy of trapped, sympathetically cooled ions. Theoretical results calculated using configuration interaction plus many-body perturbation theory (CI+MBPT), coupled cluster with single and double excitation (CCSD), and multiconfiguration Dirac–Hartree–Fock (MCDHF) methods show good agreement with experimental data, converging to nuclear moments of $\mu_g = 0.365(3)$ μ_N and $Q_g = 3.11(5)$ eb.[72] The only A constant for the isomeric state is $-267(3)$ MHz,[65] which has the opposite sign to the nuclear ground state.

Experimental studies of $^{229m}Th^{3+}$ are currently limited to laser spectroscopy work by Yamaguchi *et al.*,[65] who measured the A and B for the $6d_{3/2}$ electronic state in the nuclear isomeric state of $^{229}Th^{3+}$, yielding $-267(3)$ MHz and 1288(10) MHz, respectively. Utilizing these experimental results, they determined μ and Q of the nuclear excited state to be $-0.378(8)$ μ_N and 1.77(2) eb, respectively, representing the most precise determinations to date.

Compared to $^{229}Th^{3+}$, experimental and theoretical investigations of hyperfine structure constants and nuclear moments for $^{229}Th^{2+}$ remain relatively scarce, with primary contributions from the works of Thielking *et al.*[73] and Müller *et al.*[68] For the $^{229}Th^{2+}$ isomeric state, Thielking *et al.* reported the hyperfine structure constants as $A_m = -263(29)$ MHz and $B_m = -151(22)$ MHz for the $6d^2,^3F_2$ state, and $A_m = 53(65)$ MHz and $B_m = 498(15)$ MHz for the $5f6d,^1P_1^o$ state. Using these values, they obtained the magnetic dipole moment $\mu_m = -0.37(6)$ μ_N and the electric quadrupole moment $Q_m = 1.74(6)$ eb for the isomeric state. In the same year, Müller *et al.* performed MBPT and MCDHF calculations,[68] using experimental results from Ref. [73] to derive $\mu_m = -0.35$ μ_N and $Q_m = 1.74(8)$ eb for the nuclear excited state. These theoretical results agree well with those reported by Thielking *et al.*,[73] reinforcing the consistency of current knowledge on the nuclear properties of the isomeric $^{229}Th^{2+}$ system.

Table 2. Listed are the nuclear magnetic dipole moment μ (in μ_N), electric quadrupole moment Q (in eb). The ratios A/μ (MHz/μ_N) and B/Q (MHz/eb), and the hyperfine constants A_g, B_g, A_m, and B_m (MHz) for the $^{229}Th^{3+}$ and $^{229}Th^{2+}$ ions. In Ref. [69], two sets of μ and Q were determined by combining theoretical values from different methods with experimental data. μ_N is the nuclear magneton and 1 eb = 1.6022×10^{-47} Cm^2.[74]

	$^{229}Th^{3+}$				
	$5f_{5/2}$	$5f_{7/2}$	$6d_{3/2}$	$6d_{5/2}$	Final
A_g/μ_g theory[75]a	229.2	86.1	431.5	–36.7	
A_g/μ_g theory[69]b	232.28	87.14	442.71	–35.39	
A_g/μ_g theory[69]c	230.53	87.12	431.85	–23.31	
A_g Expt.[71]	82.2(6)	31.4(7)	155.3(12)	–12.6(7)	
A_g Expt.[72]	82.0(2)			–12.9(3)	
A_m Expt.[65]			–267(3)		
μ_g[75]	0.359	0.365	0.360	0.343	0.360(7)
μ_g[69]b	0.354(3)	0.360(8)	0.351(3)	0.365(20)	0.355(9)
μ_g[69]c	0.357(3)	0.360(8)	0.360(3)	0.241(30)	0.359(9)
μ_g[70]					0.53 – 0.66
μ_g[76]					0.54
μ_g[72]	0.365(3)				0.31(7)
μ_m[65]					–0.378(8)
μ_m[70]					–0.25––0.35
B_g/Q_g theory[77]d	740	860	690	860	
B_g/Q_g theory[75]a	725	809	738	873	
B_g/Q_g theory[69]b	743	829	746	883	
B_g/Q_g theory[69]c	783	879	758	897	
B_g Expt.[71]	2269(6)	2550(12)	2265(9)	2694(7)	
B_g Expt.[72]	2270.3(1.8)			2695.7(1.9)	
B_m Expt.[65]			1288(10)		
Q_g[75]	3.13	3.15	3.07	3.09	3.11(6)
Q_g[69]b	3.06(1)	3.07(2)	3.04(1)	3.05(1)	3.05(3)
Q_g[69]c	2.90(1)	2.90(2)	3.00(1)	3.00(1)	2.95(7)
Q_g[70]					2.80(27)
Q_g[78]					3.15(3)
Q_g[71]					3.11(16)
Q_g[72]	3.11(5)				3.10(4)
Q_m[65]					1.77(2)
Q_m[70]					1.56
	$^{229}Th^{2+}$				
	$6d^2\ ^3F_2$	$5f6d\ ^1P^o_1$	Final		
A_m/μ_m theory[68]d	660	506			
A_m/μ_m theory[68]e	749	419			
B_m/Q_m theory[68]d	22	270			
B_m/Q_m theory[68]e	23	222			
A_g Expt.[73]	151(8)	88(4)			
B_g Expt.[73]	73(27)	897(14)			
A_m Expt.[73]	–263(29)	53(65)			
B_m Expt.[73]	–151(22)	498(15)			
μ_m			–0.37(6)[73], –0.35[68]		
Q_m			1.74(6)[73], 1.74(8)[68]		

[a] from SDpT method, [b] from LCCSD method, [c] from CCSD method, [d] from CI+MBPT method, [e] from MCDHF method.

3. Electronic properties of ^{229}Th atomic systems

The nuclear transition frequency in ^{229}Th is profoundly influenced by extranuclear electron configurations through hyperfine interactions.[69,75,79] Therefore, precise knowledge of thorium's electronic structures is critical for selecting laser-accessible electronic states, designing efficient cooling schemes, and achieving high-precision quantum-state control. However, the accurate many-body calculations for ^{229}Th face significant challenges: the high atomic number ($Z = 90$) amplifies relativistic effects, strong electron correlation complicates open-shell configurations, and complex CI persists in in-

termediate charge states. These factors collectively contribute to the scarcity of reliable experimental and theoretical data for various ^{229}Th ions, particularly in the intermediate charge-state region. Given these computational challenges and the scarcity of experimental benchmarks, accurate modeling of ^{229}Th systems requires advanced relativistic many-body methods. The following subsection is a brief overview of the common and mainstream many-body theoretical methods used for such calculations.

3.1. Theoretical methods for electric structure calculations

To accurately determine the electronic structures and electric properties of ^{229}Th atoms and their ions, it is essential to employ high-precision theoretical methods capable of simultaneously accounting for both strong relativistic and complex electron correlation effects.[32,75,79–81] As thorium belongs to the actinide series of heavy elements, its electronic structure exhibits strong electron correlation effects.[82–84] Therefore, traditional non-relativistic approaches are insufficient to meet the required accuracy.[85] Currently, the most widely used high-precision theoretical methods include MCDHF, MBPT, and relativistic coupled-cluster (RCC) methods. A brief overview of these methods is provided below.

The MCDHF method optimizes both orbital functions and configuration mixing coefficients self-consistently to obtain the best variational description of atomic state wavefunctions.[86–89] The atomic state function is expressed as a linear combination of configuration state functions:[87,90,91]

$$|\Psi(\gamma J)\rangle = \sum_{i=1}^{N_{\rm CSF}} c_i |\Phi(\gamma_i J)\rangle, \tag{9}$$

where γ denotes all quantum numbers other than J, and c_i are the mixing coefficients. The self-consistent field procedure simultaneously optimizes the orbitals and coefficients c_i to minimize the total energy.[92] Subsequently, a relativistic CI calculation is usually performed, in which the configuration state function (CSF) space is expanded to include the Breit interaction and quantum electrodynamic (QED) corrections.[90–92] MCDHF provides a fully relativistic and variationally consistent description, making it highly suitable for heavy elements.

MBPT systematically incorporates electron correlation effects through perturbative expansions.[22,41,93,94] The total Hamiltonian $\hat{H}$ is decomposed as[95]

$$\hat{H} = \hat{H}_0 + \hat{V}_{\rm I}, \tag{10}$$

where $\hat{H}_0$ contains the nuclear potential and the V^{N-1} potential describing the average interaction between core and valence electrons,[83,96] and $\hat{V}_{\rm I}$ represents the residual interaction. For monovalent systems, valence correlation is often approximated by the second-order self-energy operator $\Sigma^{(2)}(E)$:

$$\left[\hat{H} + \Sigma^{(2)}(E)\right] |\psi\rangle = E|\psi\rangle, \tag{11}$$

which is derived from Brillouin–Wigner or Rayleigh–Schrödinger perturbative frameworks.[97] MBPT provides a systematic framework for including correlation effects, and when the perturbation series converges well, it yields highly accurate results. However, convergence may deteriorate in strongly correlated or near-degenerate systems, in which case non-perturbative methods are required.[84]

The RCC method systematically captures electron correlation effects of all orders through an exponential ansatz for the excitation operator.[69,98–100] The exact wavefunction is constructed as

$$|\Psi_v\rangle = {\rm e}^S |\Phi_v\rangle, \tag{12}$$

where $|\Phi_v\rangle$ represents the zeroth-order reference state, and S is the total excitation operator including single (S_1), double (S_2), and higher excitations ($S_3, \ldots$). In the commonly used CCSD approximation, only single and double excitations are retained, while including all linear and nonlinear terms arising from their exponential expansion. The linearized version, LCCSD, retains only the linear terms ($S_1 + S_2$). It should be noted that the LCCSD approach is formally equivalent to the all-order method[84,95,101] used by Safronova *et al.*, where the nonlinear coupled-cluster terms are neglected.[69,75,79,102] LCCSD is computationally efficient but slightly less accurate than CCSD.[69]

For multivalent systems, a single theoretical approach is often insufficient to accurately capture both core and valence correlations. Therefore, hybrid methods combining CI with MBPT or RCC techniques have become important tools in studying ^{229}Th systems.[68,84] Typically, core–valence correlations are computed to all orders using RCC[25,48,75,84] and incorporated into the valence-space effective Hamiltonian as Σ or $\hat{H}_{\rm eff}$. The correlations among valence electrons are then treated using the CI method,[41,80,84,103] ensuring an accurate description of both valence and core correlations. For the ^{229}Th atom and its ionic systems, CI-based hybrid approaches such as CI+all-order are typically employed to achieve the best agreement between theory and experiment.

These theoretical frameworks provide the foundation for accurate modeling of electronic structures in thorium and its ions. As summarized in Table 3, recent theoretical studies have reported various electronic structure properties for different thorium ions, with methodological details and validation benchmarks available in the corresponding references. The following subsections focus specifically on low-charged ions (^{229}Th^{+}–^{229}Th^{4+}), motivated by their experimental relevance, laser-accessible electronic configurations, and the contrasting performance of current theoretical methods in this regime.

Table 3. The electronic structure properties of ^{229}Th ions, including energy (E), Landé factor (g), lifetime (τ), transition rate (A_r), oscillator strength (f), line strength (S), reduced matrix elements of electric and magnetic multipoles ($\mathrm{RME}_{\mathrm{E}\lambda}$, $\mathrm{RME}_{\mathrm{M}\lambda}$), branching ratio ($B_r$), field shift constant (F_0), polarizability ($\alpha_{\mathrm{E}\lambda}$), transition amplitudes ($\mathrm{TA}_{\mathrm{M1}}$, $\mathrm{TA}_{\mathrm{E2}}$), radiative width ($\Gamma_{\mathrm{rad}}$), and radiative lifetime (τ_{rad}).

System	Method	Properties	Ref.
^{229}Th	CI+all-order	E, g	[84]
	CCSD+CI	F_0	[80]
^{229}Th^{+}	CI+all-order	F_0	[104]
	CCSD+CI	F_0	[80]
	CI+MBPT	E, g, τ	[96]
	CI+all-order	E, g	[84]
	CI+MBPT	E, g	[41]
	CI+MBPT	E, F_0	[77]
	HFR+CPOL/CI+MCDHF	E, f	[105]
^{229}Th^{2+}	CCSD+CI	F_0	[80]
	CI+all-order	F_0	[104]
	CIPT	F_0	[106]
	DFT	E	[107]
	CI+all-order	E, g, τ, A_r, f, B_r, $\mathrm{RME}_{\mathrm{E1}}$, $\mathrm{RME}_{\mathrm{E2}}$, $\mathrm{RME}_{\mathrm{M1}}$, $\mathrm{RME}_{\mathrm{M2}}$	[84]
	CI+MBPT	E, F_0	[77]
	CI+MCDHF	E, B_r, f, A_r	[92]
^{229}Th^{3+}	all-order/MBPT	E, $\mathrm{RME}_{\mathrm{E1}}$, $\mathrm{RME}_{\mathrm{E2}}$, $\mathrm{RME}_{\mathrm{E3}}$, $\mathrm{RME}_{\mathrm{M1}}$, $\mathrm{RME}_{\mathrm{M2}}$, $\mathrm{RME}_{\mathrm{M3}}$, f, A_r, τ, α_{E1}	[101]
	all-order/MBPT	E, $\mathrm{RME}_{\mathrm{E2}}$, $\mathrm{RME}_{\mathrm{M1}}$, f, A_r, α_{E1}	[95]
	HFR+CP	f, A_r	[108]
	HFR/HFR+CP	E, f	[109]
	TDHF+CP	g, $\mathrm{TA}_{\mathrm{M1}}$, $\mathrm{TA}_{\mathrm{E2}}$	[110]
	DF/MBPT/all-order	$\mathrm{RME}_{\mathrm{M1}}$, $\mathrm{RME}_{\mathrm{E2}}$	[111]
	CCSD	F_0	[80]
	CIPT	F_0	[106]
	SDpT/all-order/MBPT	$\mathrm{RME}_{\mathrm{E1}}$, f, τ, A_r, α_{E1}	[79]
	MBPT/DFCP	E, τ, g, $\mathrm{RME}_{\mathrm{E1}}$, $\mathrm{RME}_{\mathrm{E2}}$, $\mathrm{RME}_{\mathrm{M1}}$, A_r, B_r, α_{E1}	[97]
	MBPT	E, F_0	[77]
	LCCSD/CCSD	E	[69]
	DF/CCSD	E, g, $\mathrm{RME}_{\mathrm{E1}}$, $\mathrm{RME}_{\mathrm{E2}}$, $\mathrm{RME}_{\mathrm{M1}}$, f, S, A_r	[112]
	FSCCSD	E	[113]
^{229}Th^{4+}	CIPT	E, F_0, g	[106]
	RPA	α_{E1}	[79]
	MBPT/DFCP	α_{E1}	[97]
	FSCCSD	E	[113]
	RPA+HF	α_{E1}	[109]
	CI+all-order/MBPT	α_{E1}	[95]
	HF	α_{E1}	[114]
	CCSD(T)	α_{E1}	[115]
	CI+all-order	E, $\mathrm{RME}_{\mathrm{M1}}$, $\mathrm{RME}_{\mathrm{E2}}$, A_r, τ	[103]
	MBPT	E, $\mathrm{RME}_{\mathrm{E1}}$, $\mathrm{RME}_{\mathrm{E2}}$, $\mathrm{RME}_{\mathrm{E3}}$, $\mathrm{RME}_{\mathrm{M1}}$, $\mathrm{RME}_{\mathrm{M2}}$, $\mathrm{RME}_{\mathrm{M3}}$, S, A_r	[116]
	DF/RPA	α_{E1}, α_{E2}	[116]
^{229}Th^{35+}	DHF+CI	E	[43]
^{229}Th^{39+}	MCDHF	E	[51]
^{229}Th^{87+}	DFT	E, Γ_{rad}, τ_{rad}	[117]
^{229}Th^{88+}	CI	E	[118]
^{229}Th^{89+}	DFT	E, Γ_{rad}, τ_{rad}	[117]

3.2. ^{229}Th^{+} ion

The ^{229}Th^{+} ion, a moderately complex 89-electron system with three valence electrons, exhibits significant electron correlation effects that complicate accurate electronic structure calculations. Figure 2 illustrates its simplified energy levels diagram. To address the electron-correlation problem in this system, several advanced theoretical approaches have been employed, including CI+MBPT,[41,77,96] which incorporates second-order perturbative corrections to single-electron self-energy and screened Coulomb interactions within the relativistic Dirac–Hartree–Fock framework; CI plus all-order method (CI+all-order),[84,104] which improves correlation treatment through iterative coupled-cluster corrections; and the singles-doubles coupled-cluster method combined with CI method (CCSD+CI),[80] which offers complementary computational advantages.

The computational challenge in this system is clearly illustrated by the systematic study of Gamrath *et al.*[105] They

found that while the MCDHF+CI approach reproduces experimental energy levels reasonably well, its predicted oscillator strengths show notable discrepancies. This indicates that for heavy multi-electron systems, achieving accurate radiative transition properties remains highly challenging. A comparison of different methods is summarized in Table 4, which shows that both CI+all-order[84] and CI+MBPT[77] reproduce the low-lying level ordering well, with CI+all-order generally achieving closer agreement and CI+MBPT tending to slightly overestimate some excitation energies.

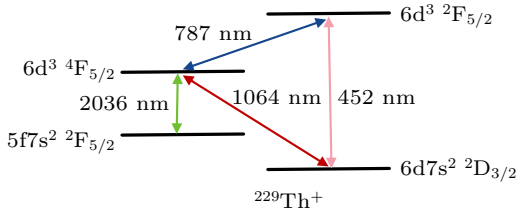


Fig. 2. Partial energy levels of the ^{229}Th$^+$ ion. All transition energies are sourced from Ref. [119].

Table 4. Energies (in cm^{-1}) of selected low-lying states of the ^{229}Th$^+$ ion.

Conf.	Term	CI+all-order[84]	CI+MBPT[77]	Expt.[77]
7s^2	^{2}F$_{5/2}$	3882	4856	4490
6d7s	^{4}F$_{3/2}$	6020	7487	6691
6d7s	^{4}F$_{5/2}$	6651	8325	7331
6d7s	^{4}G$_{5/2}$	9229	100 45	9585
6d7s	^{4}H$_{5/2}$	9978	121 68	106 73
6d7s	^{2}D$_{3/2}$	106 95	130 54	115 76
6d7s	^{4}D$_{1/2}$	115 75	128 97	117 25
6d7s	^{2}F$_{5/2}$	120 45	145 64	124 72
6d7s	^{4}F$_{3/2}$	126 57	142 33	129 02
6d7s	^{4}G$_{1/2}$	139 65	158 53	141 02

Despite these challenges, the CI+MBPT approach achieves an accuracy of ~ 100 cm^{-1} for low-lying excited states[41,96] and predicts unobserved even-parity states.[41] It also shows less than 0.5% deviation in Landé g-factors compared to experiment.[96] The CI+all-order method further reduces relative errors (e.g., from 18% to 10% for the 6d^3 ^{2}D$_{3/2}$ state).[84] Beyond energy levels, CI+MBPT enables $\sim 10\%$ accuracy radiative lifetime calculations for odd-parity states[96] and intensity-based fitting for strongly mixed states ($J = 3/2$).[96] These results illustrate the strengths and limitations of different theoretical approaches. Despite limited experimental validation for certain predictions, they provide critical insights into nuclear–electron coupling mechanisms in ^{229}Th$^+$ and related ions like ^{229}Th^{2+}.

3.3. ^{229}Th^{2+} ion

The ^{229}Th^{2+} ion, comprising 88 electrons with two valence electrons outside the closed-shell [Rn] core, represents a promising platform for nuclear optical clock development and precision tests of fundamental physics constants.[84] The simplified energy-level structure diagram is shown in Fig. 3, highlighting key laser-accessible transitions between low-lying states.

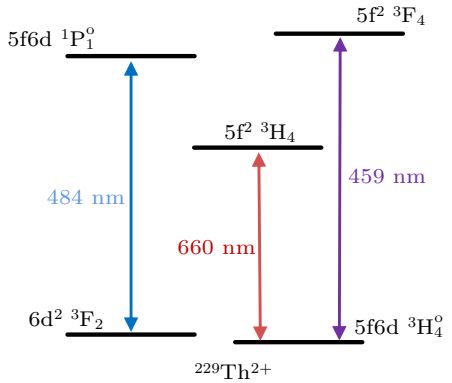


Fig. 3. Low-lying energy levels of the ^{229}Th^{2+} ion. All transition energies are sourced from Ref. [104].

Theoretical studies of ^{229}Th^{2+} have employed multiple computational approaches to address its complex electronic structure. Early work by Mazzone *et al.* utilized density functional theory (DFT) combined with coupled-cluster singles and doubles with perturbative triples (CCSD(T)) to investigate electronic configurations and chemical reactivity with water.[107] While this method provided qualitative insights into reaction mechanisms, it failed to resolve ground state configuration ordering, limiting its utility for precision spectroscopy. To improve accuracy, Safronova *et al.* employed the CI+all-order method to calculate the excitation energies, Landé g-factors, and electromagnetic dipole matrix elements with sub-1% precision.[84] For strong E1 transitions, this method demonstrated $< 2\%$ deviation from experimental measurements while maintaining computational feasibility.[84]

Table 5. Energies (in cm^{-1}) of selected low-lying states of the ^{229}Th^{2+} ion.

Conf.	Term	CI+all-order[84]	CI+MBPT[77]	Expt.[77]
6d^2	^{3}F$_3$	4938	4023	4056
6d^2	^{3}F$_4$	7264	6795	6538
6d7s	^{3}D$_3$	106 41	9204	9954
6d^2	^{1}G$_4$	108 22	110 51	105 43
5f^2	^{3}H$_4$	145 14	133 58	151 49
5f^2	^{3}H$_5$	171 31	160 68	178 87
5f^2	^{3}F$_3$	203 78	190 80	208 40
5f^2	^{3}F$_4$	217 82	203 66	217 84
5f^2	^{1}G$_4$	270 45	252 69	259 72
5f7p	^{3}G$_3$	337 15	33 402	335 62
5f7p	^{3}F$_3$	387 36	386 17	384 32

A systematic comparison of calculated and experimental energies for low-lying states of ^{229}Th^{2+} is summarized in Table 5, with more comprehensive data available in the work of Kitovienė *et al.*[92] The table shows that both CI+all-order[84] and CI+MBPT[77] calculations accurately reproduce the general ordering of 6d^2 and 6d7s configurations. For the 6d^2 ^{3}F$_3$ state, CI+MBPT yields 4023 cm^{-1}, showing a 33 cm^{-1} deviation, while for the 6d7s ^{3}D$_3$ state, the discrepancy increases

to 750 cm^{-1}. Although CI+all-order slightly overestimates excitation energies for certain states, it maintains consistent accuracy across the spectrum.

For highly-excited states involving 5f electrons, such as $5f^2$ and 5f7p, method-dependent performance diverges: CI+MBPT systematically underestimates the $^3H_4$ and $^3H_5$ levels, whereas CI+all-order reduces deviations by 30%–50%. This improvement indicates more effective modeling of f-electron correlations and core–valence interactions in the CI+all-order approach. Residual discrepancies exceeding 1000 cm^{-1} for these states likely arise from QED effects not fully considered in current methodologies.

The challenge in accurately describing highly-excited states is further underscored by Kitovienė *et al.*[92] Using the MCDHF+CI approach, they reported deviations exceeding 3500 cm^{-1} for states such as $6d^2\,^1S_0$ and $5f^2\,^1S_0$. They noted that even with the inclusion of Breit interactions and QED corrections, these states remain problematic, suggesting that very strong electron-correlation effects must be addressed in future theoretical work.

3.4. $^{229}Th^{3+}$ ion

The $^{229}Th^{3+}$ ion, characterized by a single valence electron outside closed shells, leads to a relatively simple electronic spectrum while retaining significant electron correlation and relativistic effects. Consequently, $^{229}Th^{3+}$ has become an important system for high-precision theoretical tests and nuclear clock studies, with its simplified level structure illustrated in Fig. 4.

A broad set of theoretical methods has been employed. The all-order approach[95,101] (equivalent to the LCCSD method for $^{229}Th^{3+}$ ions[102]) has been used alongside SDpT[79] to sum dominant correlation terms to all orders, enabling calculations of reduced matrix elements, oscillator strengths, transition rates, and polarizabilities. MBPT up to second and third order[79,95,101,111] has also been applied, though it tends to overestimate correlations. The LCCSD, CCSD, and Fock-space CCSD (FSCCSD) methods provide particularly accurate descriptions of strong 5f correlations, yielding reliable energies and *g*-factors.[69,112,113] The Dirac–Fock plus core polarization (DFCP) method has given accurate energies, lifetimes, polarizabilities, and *g*-factors, with average relative errors of 0.17% and a maximum of 0.59% for the $7d_{5/2}$ state.[97]

Li *et al.* performed detailed comparisons of energies, *g*-factors, and transition matrix elements among different methods (see Tables 2–8 of Ref. [69]). The standalone Dirac–Fock (DF) calculations show significant deviations from experiment, for instance incorrectly predicting the $6d_{3/2}$ and $6d_{5/2}$ levels as the lowest, in contradiction with the experimentally established $5f_{5/2}$ ground state.[69] This limitation of DF calculations in reproducing the correct level ordering has also been reported previously,[120] emphasizing the importance of correlation effects in the $^{229}Th^{3+}$ ion. The incorrect prediction of energy levels is corrected by including correlations via CCSD, with most deviations kept within a few hundred cm^{-1}.[69,112] For low-lying states, the CCSD results are consistent with those of FSCCSD, with absolute deviations within a few hundred cm^{-1}. Although the SDpT method includes partial triple excitations, significant uncertainties remain in the calculations for the 5f states.[79]

In addition to energy levels, key properties such as *g*-factors, lifetimes, and transition rates have also been extensively studied. For example, the CCSD *g*-factor of the $5f_{5/2}$ state reported by Li *et al.*[112] shows excellent agreement with values calculated using DFCP, MBPT, and all-order methods,[97] with a relative deviation of only 0.03%. Similarly the lifetime of the $5f_{7/2}$ state is consistently predicted to be around 1.07 s, with a deviation of less than 0.2%.[97]

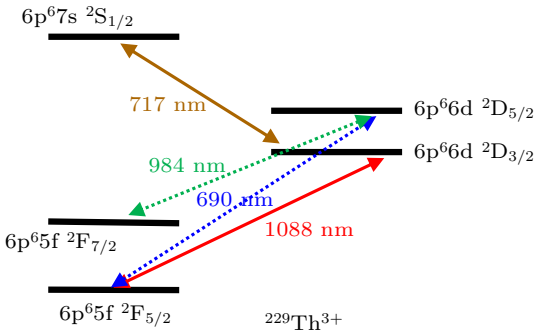


Fig. 4. Simplified levels structure of the $^{229}Th^{3+}$ ion. All transition energies are sourced from Ref. [31].

3.5. $^{229}Th^{4+}$ ion

The $^{229}Th^{4+}$ ion has a closed-shell [Rn] configuration with 86 electrons. The simplified energy-level diagram is shown in Fig. 5. A variety of theoretical methods have been employed to calculate the electronic structure properties of $^{229}Th^{4+}$, including DFCP,[95,97] MBPT,[116] the COWAN code (relativistic HF),[116] relativistic coupled-cluster approaches such as FSCCSD and CCSD(T),[113,115] the CI+all-order method,[103] and the CI plus perturbation theory (CIPT) approach[106] have systematically provided energy and multipole transition data, including reduced matrix elements, line strengths, polarizability, and transition rates.

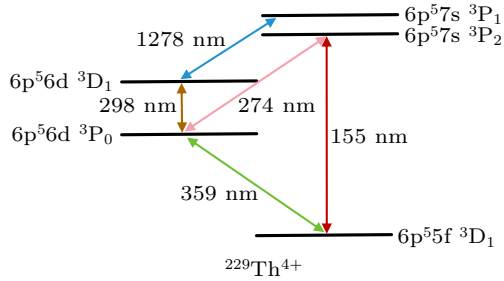


Fig. 5. Partial energy levels of the $^{229}Th^{4+}$ ion. All transition energies are sourced from Ref. [113].

Table 6 compares energies of selected low-lying states obtained by MBPT, FSCCSD, CI+all-order, and CIPT. For example, the results obtained by the FSCCSD method are in relatively good agreement with those from the CI+all-order and CIPT methods, typically within a few thousand cm^{-1}. In contrast, MBPT first- and second-order corrections predict very different values for the $6p^5\,5f\,^3D_1$ state, 140482 cm^{-1} and 103961 cm^{-1},[116] thereby highlighting the critical role of electron correlation in accurate energy-level calculations.

Owing to its closed-shell structure, the electric-dipole polarizability α_{E1} of $^{229}Th^{4+}$ has attracted particular attention. Early Hartree–Fock (HF) calculations yielded $\alpha_{E1} = 10.26$ a.u.,[114] while Safronova *et al.* reported 8.957 a.u. and 7.750 a.u. using HF and MBPT methods, respectively,[116] with the MBPT result being in excellent agreement with the experimental value of 7.720(7) a.u.[85]

Table 6. Energies (in cm^{-1}) of selected low-lying states in the $^{229}Th^{4+}$ ion from different theoretical methods.

		Ref. [116]			Ref. [113]	Ref. [103]	Ref. [106]
Conf.	Term	MBPT1	MBPT2	COWAN	FSCCSD	CI+all-order	CIPT
$6p^5 5f$	$^3D_1$	140 482	103 961	135 013	134 611	134 995	138 922
$6p^5 5f$	$^3D_2$	145 992	103 880	140 469	139 281	139 842	143 129
$6p^5 5f$	$^3G_4$	150 413	111 611	143 819	141 711	143 160	146 618
$6p^5 5f$	$^3G_5$	150 707	115 151	145 606	143 341	144 714	147 335
$6p^5 5f$	$^3F_3$	153 648	114 426	147 698	147 198	146 314	149 812
$6p^5 5f$	$^1F_3$	157 314	117 597	150 759	145 490	148 081	151 891
$6p^5 6d$	$^3P_0$	161 118	142 323	158 019	162 504	–	159 866
$6p^5 5f$	$^3F_4$	162 859	123 001	156 377	153 249	154 552	157 311
$6p^5 6d$	$^3P_1$	165 218	142 612	161 937	165 864	–	163 431
$6p^5 5f$	$^1D_2$	168 847	131 630	160 980	157 311	159 248	161 992
$6p^5 6d$	$^3F_3$	171 752	151 508	167 594	171 749	–	169 790
$6p^5 6d$	$^3D_2$	172 385	152 205	168 716	176 615	–	170 331
$6p^5 6d$	$^3F_4$	172 707	156 599	169 952	174 222	–	171 779
$6p^5 6d$	$^1D_2$	177 529	157 399	173 943	172 331	–	174 617
$6p^5 6d$	$^3D_3$	183 988	163 203	180 490	183 289	–	181 285
$6p^5 7s$	$^3P_2$	199 837	176 394	197 368	199 042	–	–
$6p^5 6d$	$^3D_1$	200 125	181 998	196 142	196 048	–	195 273
$6p^5 7s$	$^3P_1$	271 974	244 433	268 988	203 910	–	–
$6p^5 5f$	$^3G_3$	216 008	174 712	209 865	204 656	205 597	208 580
$6p^5 5f$	$^3D_3$	220 528	179 353	215 174	209 954	210 417	212 757
$6p^5 5f$	$^3G_4$	223 552	181 736	217 527	–	214 015	215 662

3.6. Other ^{229}Th ions

Beyond the extensively studied low-charged thorium ions, highly-charged ions (HCI) of ^{229}Th, such as $^{229}Th^{35+}$, $^{229}Th^{39+}$, and few-electron Th ions ($^{229}Th^{87+}$, $^{229}Th^{88+}$, $^{229}Th^{89+}$), have garnered increasing interest. This interest arises from their simple electronic spectra, which enable accurate calculations.

State-of-the-art atomic structure calculations have been performed for these systems. Porsev *et al.* employed large-scale CI with over 1.2×10^8 determinants to study $^{229}Th^{35+}$.[43] They identified a low-lying $J = 13/2$ excited state at approximately 8.40 eV above the $J = 15/2$ ground state, close to the ^{229}Th isomeric energy of 8.356 eV. This proximity enables an EB excitation rate of ~ 0.3 s^{-1} under resonance conditions. Koziol and Rzadkiewicz investigated $^{229}Th^{39+}$ using the MCDHF method.[51] With an optimized active space, they determined the first excited state ($J = 7/2$) to lie at 8.308(69) eV, in near resonance with the isomeric energy. This yields a predicted nuclear excitation by electron transition (NEET) rate of up to 2.5×10^{16} s^{-1} at exact resonance.

For few-electron ^{229}Th ions, Tkalya and Nikolaev[117] applied DFT to lithium-like $^{229}Th^{87+}$ and hydrogen-like $^{229}Th^{89+}$ (see Figs. 6 and 8 for simplified energy levels diagrams). They evaluated radiative transition width (Γ_{rad}), lifetimes (τ_{rad}), hyperfine splittings (including the Bohr–Weisskopf effect), and state mixing. Meanwhile, Yerokhin and Surzhykov[118] used relativistic CI to study helium-like $^{229}Th^{88+}$ (see Fig. 7 for simplified energy levels diagram), calculating fine-structure energies of *n*s and *n*p states and providing an uncertainty analysis consistent with available experimental results.

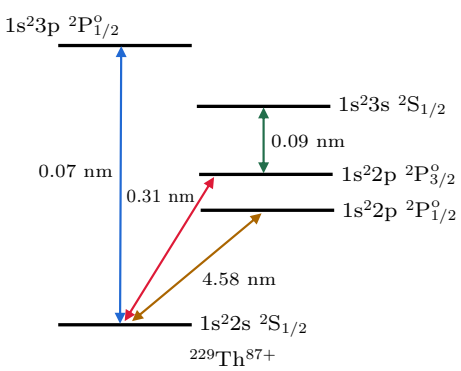


Fig. 6. Simplified energy levels of the $^{229}Th^{87+}$ ion.

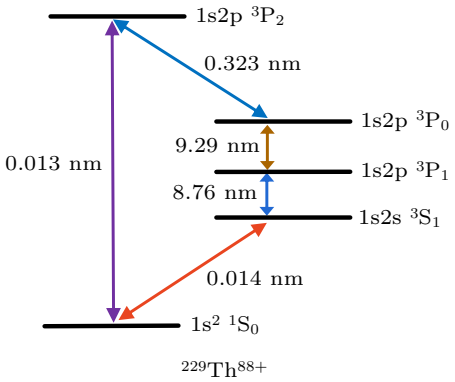


Fig. 7. Simplified energy levels of the $^{229}Th^{88+}$ ion. All transition energies are sourced from Ref. [119].

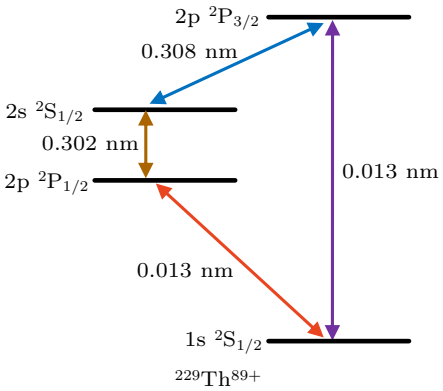


Fig. 8. Simplified energy levels of the $^{229}Th^{89+}$ ion. All transition energies are sourced from Ref. [119].

The first transition energy (in eV) of the fine-structure for different ^{229}Th ions is summarized in Table 7. For lowly charged ions such as $^{229}Th^{+}$ and $^{229}Th^{2+}$, the first excitation energy lies in the laser-accessible regime, while in HCI system, the excitation energies shift to hundreds of eV ($^{229}Th^{87+}$) and tens of keV ($^{229}Th^{88+}$, $^{229}Th^{89+}$). For example, the value obtained from the MBPT method is $E = 0.188691$ eV for $^{229}Th^{+}$, whereas the $1s \to 2p$ excitation energy in hydrogen-like $^{229}Th^{89+}$ is 92815.6 eV.[119] This value is five orders of magnitude larger than that in low-charged ^{229}Th ions, highlighting the significant impact of the degree of ionization on the excitation energies of ^{229}Th ions. The results in Table 7 also indicate that fine-structure energy matching the ~ 8.4 eV nuclear isomeric energy may exist in moderately ionized ^{229}Th ions. This prediction has been validated through theoretical studies of $^{229}Th^{35+}$[43] and $^{229}Th^{39+}$.[51]

Further insight into nuclear–electron coupling comes from hyperfine structure calculations. Table 8 lists hyperfine splittings for representative charge states. In hydrogen-like $^{229}Th^{89+}$, the $1s_{1/2}, F = 2$ state exhibits a large splitting of -0.64 eV,[121] whereas for $^{229}Th^{3+}$ ($5f_{5/2}, F = 0$) and $^{229}Th^{2+}$ ($5f6d\,^3H^o_4, F = 3/2$), the splittings are on the order of 1×10^{-5} eV.[68,71] The values in Table 8 for extreme charge states suggest that it is challenging to identify hyperfine splitting levels in different ^{229}Th ions that match the ~ 8.4 eV nuclear isomeric energy.

Table 7. The first transition energy (in eV) for the fine-structure of different ^{229}Th ions.

System	Transition	Energy	Ref.
$^{229}Th^{89+}$	$1s\ ^2S_{1/2} \to 2p\ ^2P^o_{1/2}$	928 15.60	[119]
$^{229}Th^{88+}$	$1s^2\ ^1S_0 \to 1s2s\ ^3S_1$	912 88.17	[119]
$^{229}Th^{87+}$	$2s\ ^2S_{1/2} \to 2p\ ^2P^o_{1/2}$	270.76	[119]
$^{229}Th^{3+}$	$5f6d\ ^3H^o_4 \to 5f6d\ ^3H^o_5$	1.139 8	[122]
$^{229}Th^{2+}$	$5f6d\ ^3H^o_4 \to 5f6d\ ^3H^o_5$	0.556 644	[119]
$^{229}Th^{+}$	$6d7s^2\ ^2D_{3/2} \to 6d7s^2\ ^4F_{5/2}$	0.188 691	[119]
^{229}Th	$6d^27s^2\ ^3F_2 \to 6d^27s^2\ ^3F_3$	0.355 742	[119]

Table 8. Hyperfine splitting energies ΔE (in eV) of different ^{229}Th ions.

System	State	ΔE	Ref.
$^{229}Th^{89+}$	$1s_{1/2}, F = 2$	-0.64	[121]
$^{229}Th^{3+}$	$5f_{5/2}, F = 0$	1.38×10^{-5} [a)]	[71]
$^{229}Th^{2+}$	$5f6d\ ^3H^o_4, F = 3/2$	1.19×10^{-5} [a)]	[68]

[a)] Calculated using the A and B coefficients of Refs. [68,71].

4. Electron-nuclear-interaction-induced frequency shifts

For the bare ^{229}Th nucleus, electromagnetic interactions between electrons and the nucleus can lead to changes in the electronic structure outside the nucleus, which directly influence the properties of nuclear energy states. As shown in the previous section, precise calculations of atomic electronic structure parameters, such as the g-factor, A, and B, enable the indirect determination of key nuclear structural information. Here, we emphasize that the interactions between external electrons and the nucleus induce frequency shifts in the ^{229}Th nuclear clock.

4.1. Hyperfine-interaction frequency shift

For ^{229}Th ions with varying ionization degrees, the distinct configurations of extranuclear electrons result in differing hyperfine interactions between electrons and the nucleus. These variations lead to shifts in the nuclear transition frequency, ω_N, from the ground state to the isomeric state.[25] The frequency shifts caused by hyperfine interactions can be categorized into first- and second-order effects. The first-order effect is eliminated by averaging over all hyperfine states, whereas the second-order effect persists. The second-order hyperfine structure shift is expressed as[25]

$$\Delta E_v = \sum_n \left[\frac{\langle v|\hat{H}_A|n\rangle^2}{E_v - E_n} + 2\frac{\langle v|\hat{H}_A|n\rangle\langle n|\hat{H}_B|v\rangle}{E_v - E_n} + \frac{\langle v|\hat{H}_B|n\rangle^2}{E_v - E_n} \right]. \quad (13)$$

The explicit forms of the matrix elements $\langle v|\hat{H}_A|n\rangle$ and $\langle v|\hat{H}_B|n\rangle$ are detailed in Ref. [123]. The operators $\hat{H}_A$ and $\hat{H}_B$ represent the electron–nucleus hyperfine interactions. They are written as

$$\hat{H}_A = \sum_\lambda (-1)^\lambda \mathcal{M}_{1-\lambda} T_{1\lambda}, \quad (14)$$

$$\hat{H}_B = \sum_\lambda (-1)^\lambda \mathcal{M}_{2-\lambda} T_{2\lambda}. \quad (15)$$

Table 9 presents the differences in nuclear transition frequencies $\Delta\omega_N$ among various ^{229}Th ions, as reported by Dzuba and Flambaum,[25] as well as their relative percentages compared to the total nuclear transition frequency ω_N. The authors performed hyperfine structure calculations for ^{229}Th and its ions to analyze the dependence of the nuclear clock frequency on the HFI. They found that the first-order HFI shift exhibits significant magnitude for specific hyperfine components but cancels out when averaged over all hyperfine states. The second-order HFI shift is small but it does not vanish after averaging. It is 3 to 6 orders of magnitude smaller than the shift of the nuclear frequencies due to the Coulomb electron-nucleus interaction.[25] However, it is 5 to 8 orders of magnitude larger than the projected nuclear clock accuracy of 10^{-19}.

Table 9. Second-order hyperfine-induced frequency shifts in nuclear transitions of ^{229}Th ions.[25] The numbers in square brackets stand for powers of ten.

System	$\Delta\omega_N$		$\Delta\omega_N/\omega_N$
	(MHz)	(eV)	
^{229}Th – ^{229}Th^{+}	−4.916[−2]	−2.033[−10]	−2.438[−11]
^{229}Th – ^{229}Th^{2+}	3.495[−4]	1.446[−12]	1.734[−13]
^{229}Th – ^{229}Th^{3+}	2.459[−4]	1.017[−12]	1.220[−13]
^{229}Th^{+} – ^{229}Th^{2+}	4.951[−2]	2.048[−10]	2.456[−11]
^{229}Th^{+}– ^{229}Th^{3+}	4.940[−2]	2.043[−10]	2.450[−11]
^{229}Th^{2+} – ^{229}Th^{3+}	−1.037[−4]	−4.287[−13]	−5.142[−14]

4.2. Field shift

For different ions, besides hyperfine interaction-induced frequency shifts, size-effect-induced shifts arise from variations in Coulomb potential due to differences in nuclear charge radii between ground and isomeric states. This finite nuclear size causes electrons, especially s-orbital electrons, to experience Coulomb interactions slightly deviating from the point-charge approximation. This deviation, known as the FS, can be quantitatively derived using first-order perturbation theory,[124]

$$\Delta E_{\mathrm{FS}}^{(1)} = \sum_{n\geq 0,\mathrm{even}} F_n \delta\langle r^{n+2}\rangle_{A,A'}, \tag{16}$$

where $\delta\langle r^{n+2}\rangle_{A,A'}$ is the nuclear parameter reflecting the isotopic variation of the nuclear charge distribution,[124] and F_n represents the FS electronic factor, which describes how sensitive the nuclear probability density of electron wavefunction is to variations in the nuclear charge distribution. The leading term of approximate analytical form of F_n is given by[124]

$$F_0 = \frac{2\pi}{3} Z |\psi(0)|^2, \tag{17}$$

where $|\psi(0)|^2$ denotes the total probability density of the electronic wave function at the origin and Z represents the atomic number. Dzuba and Flambaum recently employed the CCSD+CI method to calculate the FS constant for ^{229}Th^{+}, obtaining $F_0 = 49.6$ GHz/fm^2.[80] The magnitude and sign of this value are strongly influenced by valence orbital penetration.

Due to the different electronic configurations of ^{229}Th ions, the energies of nuclear transitions within these ^{229}Th ions will also exhibit variations. The resulting difference in nuclear transition frequencies between ^{229}Th ions A and B can be approximated as

$$\Delta\omega_N = (F_{0,A} - F_{0,B})\delta\langle r^2\rangle_{229\mathrm{g},229\mathrm{m}}, \tag{18}$$

where $\delta\langle r^2\rangle_{229\mathrm{g},229\mathrm{m}}$ represents the change in the nuclear root-mean-square radius between the nuclear ground and isomeric states, $F_{0,A}$ and $F_{0,B}$ are the FS factors for the electronic ground state of ^{229}Th ions A and B, respectively.

As detailed in Table 10, the nuclear transition frequency ω_N of ^{229}Th ions exhibits significant dependence on the charge state. Dzuba and Flambaum[106] theoretically demonstrated that the relative frequency shift between ^{229}Th^{3+} and ^{229}Th^{4+} reaches $\Delta\omega_N/\omega_N \approx -2.8\times10^{-7}$, corresponding to an absolute shift of approximately −570 MHz. This shift exceeds the projected 10^{-19} fractional uncertainty target for nuclear clocks by twelve orders of magnitude. It is worth noting that the shift does not contribute to the uncertainty budget. It only indicates that the nuclear transition frequency differs among thorium systems. The phenomenon originates from the Coulomb interaction between atomic electrons and the nucleus.[80,106] To precisely quantify this effect, Si *et al.*[91] employed a non-perturbative MCDHF approach, revealing that the nuclear clock transition frequency in ^{229}Th^{3+} is 639(1) MHz lower than in ^{229}Th^{4+}. In addition to research targeting low-charge-state Th ions, Perera *et al.*[125] have also calculated the FSs for all noble-gas-like thorium ions, with the relevant data presented in Table 10. By analyzing their data, it can be observed that, among noble-gas-like thorium ions, the FS exhibits a cumulative effect with respect to the electron count, gradually increasing as the degree of ionization decreases.

Table 10. Field shift $\Delta\omega_N$ (in GHz) in the nuclear transition frequency ω_N between different ^{229}Th ions, where the latest high-precision measurement $\omega_N = 2020407384.335(2)$ GHz is used.[28] The numbers in square brackets stand for powers of ten.

System	$\Delta\omega_N$	$\Delta\omega_N/\omega_N$
^{229}Th^{88+} – ^{229}Th^{90+}	1.632[4][a]	
^{229}Th^{80+} – ^{229}Th^{90+}	1.927[4][a]	
^{229}Th^{72+} – ^{229}Th^{90+}	2.005[4][a]	
^{229}Th^{54+} – ^{229}Th^{90+}	2.021[4][a]	
^{229}Th^{36+} – ^{229}Th^{90+}	2.026[4][a]	
^{229}Th^{4+} – ^{229}Th^{90+}	2.1[4][b], 2.014[4][a]	1.0[−2][b]
^{229}Th^{3+} – ^{229}Th^{4+}	−0.57[b] , −0.639[c]	−2.8[−7][b]
^{229}Th^{2+} – ^{229}Th^{3+}	−0.15[b]	−7.4[−8][b]
^{229}Th^{+} – ^{229}Th^{2+}	1.3[b]	6.4[−7][b]
^{229}Th – ^{229}Th^{+}	0.1[b]	5[−8][b]

[a]Ref. [125]; [b]Ref. [106]; [c]Ref. [91].

5. External field effects

When considering the nucleus and electron as an integrated system, environmental perturbations such as electromagnetic fields, laser fields, and thermal gradients can alter the strength of nucleus–electron interactions, leading to shifts in nuclear transition energy. This phenomenon is referred to as external field effects. The natural shielding by outer electrons is expected to suppress systematic uncertainties from oscillating (AC) Stark, electric quadrupole, Zeeman, and blackbody radiation (BBR) shifts to the 10^{-19} level.[22] However, recent studies identify the AC Zeeman shift as a critical systematic effect, exceeding other shifts and the target uncertainty by orders of magnitude.[23] Therefore, accurately evaluating external field effects in various ^{229}Th ions is essential for the development of a high-precision ^{229}Th nuclear clock.

5.1. Zeeman shift

Ion traps inherently generate parasitic radiofrequency (rf) magnetic fields ($\boldsymbol{B}_\perp$) perpendicular to the static (DC) field ($\boldsymbol{B}$). While DC Zeeman shifts are suppressible via Zeeman averaging,[126] this fails for AC Zeeman shifts,[127] which are governed by M1 polarizabilities,

$$\Delta E = -\frac{1}{4}(\beta_\parallel \boldsymbol{B}_\parallel^2 + \beta_\perp \boldsymbol{B}_\perp^2), \tag{19}$$

where $\boldsymbol{B}_\parallel$ and $\boldsymbol{B}_\perp$ are rf field components parallel and perpendicular to $\boldsymbol{B}$, respectively. The polarizabilities $\beta_\parallel$ and $\beta_\perp$ are defined as

$$\begin{aligned}\beta_\parallel &= -\sum_{\gamma' F' m'_F}\sum_{\sigma}\frac{|\langle\Psi_{\gamma F m_F}|\mu_0|\Psi_{\gamma' F' m'_F}\rangle|^2}{E_{\gamma F m_F} - E_{\gamma' F' m'_F} + \sigma\hbar\omega},\\ \beta_\perp &= -\frac{1}{2}\sum_{\gamma' F' m'_F}\sum_{\sigma q}\frac{|\langle\Psi_{\gamma F m_F}|\mu_q|\Psi_{\gamma' F' m'_F}\rangle|^2}{E_{\gamma F m_F} - E_{\gamma' F' m'_F} + \sigma\hbar\omega}.\end{aligned} \tag{20}$$

Here μ_q is spherical components of $\boldsymbol{\mu}$ ($q=0$ aligned with $\boldsymbol{B}$), σ and q take on the values ±1 in the summations, ω denotes the angular frequency of the field and $\hbar$ is the reduced Planck constant, while $\Psi_{\gamma F m_F}$ and $E_{\gamma F m_F}$ represent wave functions and energies of hyperfine states. The magnetic dipole operator $\boldsymbol{\mu}$ is

$$\boldsymbol{\mu} = g_I \mu_N I - g_J \mu_B J, \tag{21}$$

where g_I and g_J are the nuclear and electronic g-factors, μ_N and μ_B are the nuclear magneton and Bohr magneton, and I and J are the nuclear and electronic total angular momenta.

The $^{229}Th^{4+}$ ion's electronic ground state ($J=0$) fundamentally suppresses AC Zeeman shifts in ion traps, as its lack of mixable electronic states via AC magnetic fields leaves only a negligible first-order nuclear-spin-induced shift (±0.04 Hz/μT). Averaging symmetric Zeeman components[106] can further cancel this residual effect, highlighting the ion's suitability for precision metrology. In contrast, the $^{229}Th^{3+}$ system exhibits significantly larger Zeeman shifts due to its electronic structure,[23] leading Beloy *et al.* to propose three mitigation strategies: operating the nuclear clock at a magic magnetic field $\boldsymbol{B}^*$ to suppress AC Zeeman shifts, regulating perpendicular magnetic fields ($\boldsymbol{B}_\perp$) to μT precision near $\boldsymbol{B}^*$ to minimize residual effects, and employing frequency-difference stabilization or rf spectroscopy for calibration. Despite nuclear clocks being inherently designed to suppress systematic shifts, electronic contributions to AC Zeeman shifts remain significant, with rf field sensitivity comparable to or exceeding that of conventional ion optical clocks.[23]

5.2. Nuclear electric quadrupole shift

Solid-state nuclear clocks, created by doping ^{229}Th into wide-bandgap crystals (e.g., CaF_2, $LiSrAlF_6$),[27,62,128–131] offer significant advantages: high thorium density ($\approx 10^{18}$ cm^{-3}) for improved stability, Lamb–Dicke confinement suppressing recoil and Doppler shifts, and inherent insensitivity to electromagnetic perturbations ideal for portability. However, the crystal environment induces a temperature-dependent electric quadrupole shift.

The quadrupole shift originates from the interaction between the nuclear quadrupole moment and an external electric field gradient (EFG). For a single trapped ^{229}Th ion clock, where the shift is dominated by the axial confinement field of the trap, this effect is negligible.[22] However, in solid-state materials, it becomes significant due to the crystal EFG interacting with the nuclear quadrupole moment.[28] The Hamiltonian is described as[28,29,132]

$$H = \frac{Q_\alpha V_{zz}}{4I(2I-1)}[3I_z^2 - I^2 + \eta(I_x^2 - I_y^2)], \tag{22}$$

where Q_α is the nuclear quadrupole moment, with $\alpha = g, m$ denoting nuclear ground and isomeric states, respectively. I_x, I_y, and I_z are components of nuclear angular momentum, with I as its magnitude. V_{zz} is the maximum value of the z-component EFG, and $\eta = |V_{xx} - V_{yy}|/V_{zz}$ represents the asymmetry parameter.

A non-zero η induces state mixing in quadrupole levels, altering transition strengths. In CaF_2 crystals, ^{229}Th nuclei experience strong EFG effects from surrounding lattice ions and fluorine interstitials, resulting in electric quadrupole splitting on the order of hundreds of MHz.[28] Experimental measurements reveal that both V_{zz} and η decrease with increasing temperature. For example, from 150 K to 293 K, V_{zz} decreases by 1.2% while η decreases by 3.3%. This temperature dependence is a critical systematic effect for solid-state clock operation and requires careful consideration.[29]

To mitigate these effects, solid-state nuclear clocks can suppress the fractional shift to the 10^{-19} level by rotating the

electric field direction to the magic angle and averaging over m_F sublevels.[133] Cubic symmetry crystals, like ThO_2,[64] exhibit $V_{zz} = 0$ under ideal conditions, which suppresses EFG effects and enhances clock performance.[63] For non-cubic hosts like CaF_2, recently, Zhang *et al.* directly excited the nuclear clock transition in ^{229}Th doped CaF_2 host materials using a VUV frequency comb, precisely measuring the nuclear quadrupole splitting. Through proper averaging of the quadrupole splitting pattern, the unsplit transition frequency free from EFG effects can be recovered.[28]

5.3. Stark shift

The Stark shift describes energy-level displacements caused by atomic polarization in external electric fields, such as those from trapping fields, probe lasers, or cooling lasers. Due to the extremely small nuclear differential polarizability ($< 10^{-14}\, a_0^3$) and the effective shielding of DC electric fields at the nuclear site by surrounding electron clouds, the direct nuclear contribution to DC Stark shifts is negligible. For AC electric fields, the $^{229}Th^{3+}$ nuclear clock still benefits from favorable conditions. Since E1 transitions must change parity, the AC Stark effect produces no intramanifold contribution. Consequently, the $^{229}Th^{3+}$ nuclear clock exhibits intrinsic immunity to AC Stark shifts.[23] The Stark energy shift can be expressed as

$$\Delta E_{\text{stark}} \approx -\frac{1}{2}\left[\Delta\alpha_{\text{N}} + \Delta\alpha_{\text{e}}\right]\mathcal{E}^2, \tag{23}$$

where $\Delta\alpha_{\text{N}}$ and $\Delta\alpha_{\text{e}}$ denote the differential polarizabilities of the nuclear and electron respectively, and $\mathcal{E}$ is the external electric field strength. In addition to the above-mentioned factors affecting the $^{229}Th^{3+}$ nuclear clock, the shielding effect of electrons on external electric fields in ions is also an important aspect to consider. Dzuba *et al.* pointed out that the shielding factor of electrons against external electric fields can be roughly estimated as Z_{i}/Z, where Z_{i} is the ion charge. For higher charge-state ions, electron shielding of external electric fields is generally stronger. For example, in the case of the $^{229}Th^{4+}$ ion $Z_{\text{i}}/Z = 4/90$. This enhanced shielding further suppresses the effect of static or low-frequency electric fields acting on the nucleus.[106]

In addition to the intrinsic suppression mechanisms discussed above, there are also other techniques available to further suppress Stark shifts. Averaging over m_F sublevels can eliminate electric quadrupole shifts. Under this condition, the contribution of the tensor polarizability to AC Stark shifts is also removed.[97] Furthermore, the super-Ramsey interrogation scheme provides additional suppression of AC Stark shifts.[97,134] Nevertheless, in ion traps, stray electric fields displace ions from the rf potential minimum, generating excess micromotion that induces Stark shifts.[22] For $^{229}Th^{3+}$ ions cooled to 1 mK with a 2 MHz secular frequency, this micromotion-induced AC Stark fractional shift is estimated at -1×10^{-22}. Owing to the large mass of the ion and its small differential scalar polarizability, such micromotion-induced shifts can be further suppressed to 10^{-19} level.[97]

5.4. BBR shift

The BBR shift scales with the fourth power of temperature T, and is proportional to the differential scalar polarizability,[22]

$$\Delta E_{\text{BBR}} \approx -\frac{\alpha^3\pi^3}{15}\left[\Delta\alpha_{\text{N}}^{\text{S}} + \Delta\alpha_{\text{e}}^{\text{S}}\right]T^4, \tag{24}$$

where α is the fine structure constant, $\Delta\alpha_{\text{N}}^{\text{S}}$ and $\Delta\alpha_{\text{e}}^{\text{S}}$ denote the differential scalar polarizabilities of the nuclear and electron respectively. For $^{229}Th^{3+}$ ion, the direct nuclear contribution to this shift is negligible due to minimal differential nuclear polarizability and effective electron-cloud shielding of DC electric fields at the nucleus.[22] In $^{229}Th^{4+}$ ion, Dzuba *et al.*[106] introduced an effective nuclear differential polarizability $\Delta\alpha_{\text{N}}^{\text{S}} \approx (4/90)^2\delta\langle r^2\rangle$ fm $\approx 2 \times 10^{-5}$ fm^3 $\approx 1.3 \times 10^{-19}\, a_0^3$, where the mean-square radius differnce between the clock states is $\delta\langle r^2\rangle_{229\text{g},229\text{m}} = 0.0105(13)\,\text{fm}^2$. This nuclear polarizability is orders of magnitude smaller than typical electronic polarizabilities in atomic transitions, justifying the neglect of direct nuclear contributions. The BBR shift is therefore dominated by the electric monopole mechanism. For $^{229}Th^{3+}$ at $T = 300$ K, the scalar differential polarizability $\Delta\alpha_{\text{e}}^{\text{S}} = -4 \times 10^{-5}\, a_0^3$ yields a fractional clock shift $< 1.3 \times 10^{-22}$, several orders of magnitude below conventional atomic clocks.[22] In $^{229}Th^{4+}$ ion, the closed-shell electronic structure further makes smaller differential polarizability ($\Delta\alpha_{\text{e}}^{\text{S}} = -1 \times 10^{-6}\, a_0^3$), which suppresses the BBR shift as low as $\sim 4.3 \times 10^{-24}$ at $T = 300$ K.[106]

6. Electronic bridge process for ^{229}Th nuclear clock

In the field of solid-state nuclear optical clock research, the excitation and detection of nuclear transitions have been successfully achieved based on crystalline or thin-film materials.[26–28,62,63] However, the research progress on nuclear clock based on trapped thorium ions has been relatively slow, primarily due to the current lack of effective nuclear excitation schemes. The core issue lies in the fact that although theoretical concepts for nuclear excitation have been proposed, they have not yet been experimentally validated, thus necessitating high-precision control technologies to advance this field.

For laser-implemented nuclear optical clocks, it is essential to achieve effective excitation, closed-loop control, and locking of nuclear clock transitions. Despite various theoretical schemes for electron-mediated nuclear excitation having

been proposed, such as nuclear excitation by electron capture (NEEC),[135,136] nuclear excitation by inelastic electron scattering (NEIES),[137] and recollision-induced nuclear excitation (RINE),[138–140] they all rely on strong laser fields and require precise control of laser parameters, such as field intensity, wavelength, and pulse interaction time, to enhance nuclear excitation efficiency.

However, despite these theoretical advantages, all current proposals remain experimentally unverified due to the constraints mentioned above, as well as low excitation efficiency. In contrast, although the EB mechanism process still requires precise laser control to excite electrons to high-energy states (or virtual states), it has emerged as a primary research focus due to its theoretical feasibility and comparatively simpler laser parameters. During the excitation, energy is transferred to the nucleus via radiative decay, thereby inducing a transition from the nuclear ground state to the first excited state. Crucially, the EB approach demonstrates significantly higher efficiency than direct laser excitation — particularly for trapped Th-ion nuclear clocks — with a key advantage lying in its elimination of strict energy-matching requirements between atomic and nuclear transitions; any energy mismatch is compensated through photon emission or absorption. Nevertheless, experimental confirmation of this scheme has yet to be achieved.

6.1. EB mechanism

The EB process is illustrated by the two Feynman diagrams in Fig. 9. When the initial electronic state i and the final state f have opposite parity, the process involves the emission or absorption of an electric dipole photon, in which case the EB probability is much higher than that for transitions between states of the same parity. Moreover, since the intermediate states n can span all energy levels allowed by the selection rules, the process provides multiple enhancement channels.

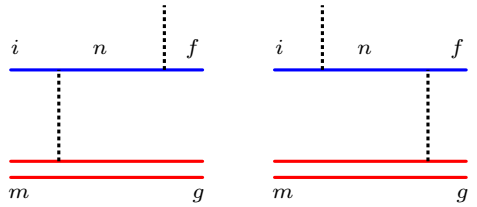


Fig. 9. Feynman diagrams of the EB process. The blue and red solid lines relate to the electronic and the nuclear transitions, respectively. The dashed line is the photon line.

The probability $\Gamma_{\rm EB}$ of the electronic dipole transition is given by[120]

$$\Gamma_{\rm EB} = \frac{4}{3}\left(\frac{\omega}{c}\right)^3 |\boldsymbol{D}_{\rm EB}|^2, \tag{25}$$

where the photon frequency ω satisfies energy conservation, $\omega = \varepsilon_i - \varepsilon_f + \omega_{\rm N}$. For simplicity, hyperfine splitting is neglected, the amplitude $\boldsymbol{D}_{\rm EB}$ is expressed as[120]

$$\begin{aligned}\boldsymbol{D}_{\rm EB} = &\sum_{K\lambda}(-1)^{\lambda}\left[\sum_n \frac{\langle f|\boldsymbol{D}|n\rangle\langle n|T_{K-\lambda}|i\rangle}{\omega_{in}+\omega_{\rm N}}\right.\\ &\left.+\sum_k \frac{\langle f|T_{K-\lambda}|k\rangle\langle k|\boldsymbol{D}|i\rangle}{\omega_{fk}-\omega_{\rm N}}\right]\langle g|\mathcal{M}_{K\lambda}|m\rangle,\end{aligned} \tag{26}$$

where $\omega_{ab} = \varepsilon_a - \varepsilon_b$. Averaging over the initial electronic states and applying the Wigner–Eckart theorem, $\Gamma_{\rm EB}$ decomposes into multipole contributions as $\Gamma_{\rm EB} = \sum_K \Gamma_{\rm EB}^{(K)}$, where $\Gamma_{\rm EB}^{(K)}$ can be represented by

$$\begin{aligned}\Gamma_{\rm EB}^{(K)} = &\frac{4}{3}\left(\frac{\omega}{c}\right)^3 \frac{\left|\langle I_{\rm g}\|\mathcal{M}_K\|I_{\rm m}\rangle\right|^2}{(2K+1)(2I_{\rm m}+1)(2J_i+1)}\\ &\times\left(\mathrm{G}_1^{(K)}+\mathrm{G}_{12}^{(K)}+\mathrm{G}_2^{(K)}\right),\end{aligned} \tag{27}$$

where

$$G_1^{(K)} \equiv \sum_{J_n}\frac{1}{2J_n+1}\left|\sum_{\gamma k}\frac{\langle\gamma_f J_f\|D\|\gamma_k J_n\rangle\langle\gamma_k J_n\|T_K\|\gamma_i J_i\rangle}{\omega_{ik}+\omega_{\rm N}}\right|^2, \tag{28}$$

$$\begin{aligned}G_{12}^{(K)} \equiv &\,2\sum_{J_t J_n}(-1)^{J_t+J_n}\left\{\begin{array}{ccc} J_i & J_t & 1\\ J_f & J_n & K\end{array}\right\}\\ &\times\sum_{\gamma_k}\frac{\langle\gamma_f J_f\|D\|\gamma_k J_n\rangle\langle\gamma_k J_n\|T_K\|\gamma_i J_i\rangle}{\omega_{ik}+\omega_{\rm N}}\\ &\times\sum_{\gamma_s}\frac{\langle\gamma_f J_f\|T_K\|\gamma_s J_t\rangle\langle\gamma_s J_t\|D\|\gamma_i J_i\rangle}{\omega_{fs}-\omega_{\rm N}},\end{aligned} \tag{29}$$

$$G_2^{(K)} \equiv \sum_{J_n}\frac{1}{2J_n+1}\left|\sum_{\gamma_k}\frac{\langle\gamma_f J_f\|T_K\|\gamma_k J_n\rangle\langle\gamma_k J_n\|D\|\gamma_i J_i\rangle}{\omega_{fk}-\omega_{\rm N}}\right|^2. \tag{30}$$

The terms $G_1^{(K)}$ and $G_2^{(K)}$ represent the contributions of the first and second Feynman diagrams in Fig. 9, respectively, while $G_{12}^{(K)}$ describes their interference. Enhancement factors $\beta_{\rm M1}$ and $\beta_{\rm E2}$ relative to M1 and E2 nuclear decay channels are defined, respectively, as

$$\beta_{\rm M1} = \left(\frac{\omega}{\omega_{\rm N}}\right)^3\frac{1}{3(2J_i+1)}\left(G_1^{(1)}+G_{12}^{(1)}+G_2^{(1)}\right), \tag{31}$$

$$\beta_{\rm E2} = \left(\frac{\omega}{\omega_{\rm N}}\right)^3\frac{1}{k_{\rm N}^2}\frac{4}{(2J_i+1)}\left(G_1^{(2)}+G_{12}^{(2)}+G_2^{(2)}\right), \tag{32}$$

where $k_{\rm N} = \omega_{\rm N}/c$. Using the known ratio of the nuclear M1 and E2 widths, $\gamma = \Gamma_{\rm N}({\rm E2})/\Gamma_{\rm N}({\rm M1}) = 6.9\times10^{-10}$,[141] the total enhancement factor can be written as $\beta = \beta_{\rm M1} + \gamma\beta_{\rm E2}$.

6.2. EB scheme for the $^{229}Th^{3+}$ ion

The trapped-ion nuclear clock based on $^{229}Th^{3+}$ relies on precise control of both ground state ($^{229g}Th^{3+}$) and isomeric state ($^{229m}Th^{3+}$) ions. While $^{229g}Th^{3+}$ ion generated via laser ablation of $^{229}Th(NO_3)_4$ and $^{229m}Th^{3+}$ ion produced from ^{233}U sources have been successfully confined in ion traps,[65,71] major challenges remain, most notably the nuclear

transition frequency of trapped ^{229}Th ions has not yet been experimentally determined due to the absence of nuclear excitation in ion-trap environments. Recent measurements of the $^{229m}Th^{3+}$ lifetime and hyperfine constants[65] provide critical parameters for clock development, but direct nuclear excitation is still required for practical applications.

To circumvent direct nuclear excitation, theoretical efforts have focused on optimizing EB and laser-induced EB (LIEB) processes. Li *et al.* illustrated the schematic energy level diagram and EB process in their 2023 work, elucidating the coupling pathways between electronic and nuclear excitations.[31] A detailed diagram of the EB scheme is provided in Fig. 1 of the referenced work. Early EB models showed that appropriate laser frequencies could enhance coupling efficiency by several orders of magnitude,[52,142] while relativistic many-body calculations revealed EB-to-radiative transition probability ratios ranging from 0.01–0.1 for $5f_{5/2} \rightarrow 6d_{3/2}, 6d_{5/2}, 7s$, and up to 20 for $7s \rightarrow 7p_{1/2}, 7p_{3/2}$ transitions.[102] However, the revised value of ~ 8.4 eV (previously assumed to be 7.6 eV) for the nuclear isomer energy necessitates recalculations using higher-accuracy methods like coupled-cluster theory. A significant advancement was the LIEB proposal,[42] in which dual-photon absorption (one from nuclear deexcitation and one from an external laser) can lead to enhancements of up to 10^8 for transitions such as $7s \rightarrow 8p_j$ in $^{229}Th^{3+}$ at nuclear energies around 8–12 eV, providing a promising route toward observable nuclear excitation.

Practical realization of ^{229}Th nuclear clocks demands precise control over ion cooling and electronic state preparation. Doppler cooling of $^{229g}Th^{3+}$ has been demonstrated via $5f_{5/2} \leftrightarrow 6d_{3/2}$ (1088 nm) or three-level $5f_{5/2} \leftrightarrow 6d_{5/2} \leftrightarrow 5f_{7/2}$ transitions (690 nm/984 nm).[31,72] Numerical simulations suggest optimal EB/LIEB pathways: initial $7s_{1/2}$ state coupled to final $7p_{1/2}$ or $8p_{1/2}$ states maximizes M1 electronic transition probabilities.[42,120] Critical unresolved issues include (1) experimental verification of LIEB-enhanced nuclear excitation rates, (2) mitigation of systematic shifts from laser-ion interactions, and (3) integration of these methods into compact trap architectures. Addressing these challenges will determine the feasibility of ^{229}Th based nuclear clocks as ultra-precise sensors for new physics beyond the Standard Model.

Building upon these theoretical pathways, recent progress has further extended the understanding of the EB in $^{229}Th^{3+}$ by explicitly incorporating hyperfine interactions. Wang *et al.*[143] developed a quantum-optical framework that treats the hyperfine electronic bridge (HEB) excitation nonperturbatively, providing new insights into the efficiency limits and control strategies of nuclear excitation. Their results indicate that dynamic coupling schemes, such as stimulated Raman adiabatic passage, can substantially enhance the population transfer efficiency, suggesting a promising pathway toward coherent nuclear-state manipulation in trapped $^{229}Th^{3+}$ systems.

6.3. EB scheme for the $^{229}Th^{2+}$ ion

The doubly charged thorium ion $^{229}Th^{2+}$ possesses a relatively simple electronic structure with two valence electrons above a closed-shell core, making it amenable to accurate theoretical modeling. At the same time, its spectral complexity remains sufficient to enable strong EB enhancement effects, a key requirement for practical nuclear excitation schemes.

Theoretical investigations have identified two primary EB pathways in $^{229}Th^{2+}$. One is the two-step excitation model proposed by Dzuba and Flambaum,[144] where the ion is first pumped to an intermediate state t (with energy E_t) via a strong E1 transition using a primary laser (ω_1). A second laser then drives the system to a final state s (with energy E_s), satisfying energy conservation relation: $\omega_1 + \omega_2 = \omega_N + E_s$. Notably, large enhancement factors (on the order of 10^4–10^5) demonstrate the efficiency of this approach. A critical parameter for optimizing this scheme is the energy denominator $\Delta = E_n - E_s - \omega_N$, where E_n and E_s denote electronic state energies of the intermediate electronic state and the final state, respectively. For example, an optimal case was identified for $t = 5f7p(J=4)$, $n = 5f7d(J=3)$, and $s = 5f6d(J=3)$ states,[144] yielding an enhancement factor $\beta = 10014$. Detailed parameters for these states, including energies, laser frequency, energy difference, and the specific enhancement factor, are listed in Table 11.

An alternative EB scheme was suggested by Müller *et al.*,[146] where nuclear excitation occurs during the decay of a high-lying electronic state, (e.g., $5f7d(J=2$ or $J=3)$) to the low-lying metastable state $6d^2(J=2)$, with the excess energy emitted as a photon. While the enhancement factor in this scheme is lower due to the relatively low energy of the emitted photon,[144] it provides the distinct advantage of enabling controlled nuclear isomer excitation via hyperfine interactions.[146]

Table 11. The EB process with resonance nuclear excitation involves three key electronic states.[144,145] Notations t, n, and s represent the intermediate state excited from the ground state via the first laser with laser energy ω_1, the virtually excited state populated by the second laser with laser energy ω_2, and the final electronic state, respectively. The energy detuning is defined as $\Delta = E_n - E_s - \omega_N$, where the nuclear transition energy $\omega_N = 67393.34$ cm^{-1}. The total enhancement factor $\beta = \beta_{M1} + \gamma\beta_{E2}$. For $^{229}Th^{2+}$, it is assumed that $E_t = 38580$ cm^{-1}. For $^{229}Th^{+}$, it is assumed that $E_t = 36390.53$ cm^{-1}.

Ions	t	n	s	E_n	E_s	ω_2 (cm^{-1})	Δ (cm^{-1})	β
$^{229}Th^{2+}$	5f7p ($J=4$)	5f7d ($J=3$)	5f6d ($J=3$)	828 27	154 53	442 66	–19	100 14
$^{229}Th^{+}$	$6d^27p + 5f6d^2$ ($J=3/2$)	($J=3/2$ or $5/2$)	$6d^27s$ ($J=1/2$)	736 37.54	6244.29	372 47.10	–0.09	1.6×10^5

6.4. EB scheme for the $^{229}Th^{+}$ ion

The $^{229}Th^{+}$ ion possesses a complex electronic structure featuring three valence electrons and an ionization potential of approximately 12 eV. This system offers a unique platform for nuclear clock development based on EB mechanisms. The high density of states in $^{229}Th^{+}$ creates a electronic transitions close to the nuclear isomer energy (~ 8.4 eV). However, the resulting spectral congestion poses a significant challenge for the precise classification of energy levels, including the determination of orbital angular momenta for excited states.

Pioneering work by Porsev *et al.* demonstrated, using the CI+MBPT method, that a two-photon resonant EB process in $^{229}Th^{+}$ could excite the nuclear state with an estimated rate of $\sim 10\ s^{-1}$.[40] Recently, Dzuba and Flambaum proposed an atomic excitation scheme that maximizes the EB effect and to estimate the magnitude of this effect.[145] With the smallest energy difference being $\Delta = -0.09\ cm^{-1}$ and a proper selection of laser frequencies, the maximum enhancement factor reached to 1.6×10^5, the corresponding atomic states and other parameters are given in Table 11. Additionally, they showed that the interaction with electrons significantly shortens the lifetime of the nuclear excited state.

6.5. EB schemes for other ^{229}Th ions

For other ^{229}Th ions, theoretical and experimental studies remain scarce, and no systematic EB excitation schemes have been developed. To date, Bilous *et al.* have reported preliminary explorations of EB processes in the $^{229}Th^{35+}$ ion.[147] Their approach specifically addressed bound-state EB processes, in which an inner-shell electron transfers absorbed photon energy to the nucleus through intermediate states. In addition, Wang *et al.*[148] extended the concept of HEB excitation to highly charged thorium ions. They identified laser-accessible HEB transitions between hyperfine levels in $^{229}Th^{32+}$ and $^{229}Th^{40+}$, which exhibit exceptionally high sensitivities to variations of the fine-structure constant. These results suggest that highly charged ^{229}Th ions may serve as promising candidates for next-generation nuclear clocks and for precision tests of fundamental physics.

7. Challenges and prospects

This review has provided a comprehensive overview of key advancements in the ^{229}Th nuclear optical clock. We traced the historical progress in precisely determining nuclear transition energy, examined the current research landscape of the ^{229}Th nuclear structure, and reviewed both progress and challenges in electronic structure studies of various thorium ions. We also summarized the EB nuclear excitation schemes which aim at the realization of a Th nuclear clock based on trapped ^{229}Th ions.

In the future, the further promotions of ^{229}Th nuclear optical clocks will depend on the synergistic progress between theoretical and experimental research, as well as the interdisciplinary integration of atomic physics, optical physics, and nuclear physics. Crucially, further progress necessitates high-precision theoretical calculations that encompass both the electronic structure of thorium ions and the nuclear structure of the ^{229}Th isomer state.

Significant challenges persist in the electronic structure calculations of ^{229}Th ions. For example, the computed wavefunctions for excited states often fail to accurately reproduce experimental energies, and the specific mechanisms of electronic coupling for certain key states remain unclear. Overcoming these is paramount, as precise electronic structure data is essential both for identifying viable resonant EB processes thus to enhance nuclear excitation rates and for accurately evaluating the uncertainties of the nuclear clock transition to external field effects.

A critical bottleneck also exists in nuclear structure theory: no existing nuclear model can accurately predict the ^{229}Th nuclear isomer energy (~ 8.4 eV). This deficiency underscores the urgent need to develop more effective nuclear theoretical methods. Precise nuclear parameters, including the energy of the isomer, transition probabilities, and the formation mechanism of its low-lying state, are vital not only for understanding the nucleus itself but also for elucidating electron-nucleus coupling mechanisms and enabling the practical development of nuclear clocks.

Building upon recent confirmations of the ^{229}Th isomer transition, this review outlines transformative pathways enabled by emerging capabilities. In the solid-state ^{229}Th system, the nuclear transition frequency with a kHz precision has been achieved benefiting from VUV frequency-comb techniques. Even higher accuracy is expected for trapped-ion clocks via novel EB nuclear excitation schemes. However, the synergistic development of low-perturbation thorium-doped crystals and environmental-shift suppression protocols will establish the foundation for functional nuclear clocks. Concurrently, advances in relativistic many-electron theory and constrained nuclear models will address fundamental challenges in electron-nucleus coupling dynamics and isomeric state formation. These developments will unlock pioneering applications in next-generation frequency metrology, tests of fundamental constant variations beyond the standard model, and quantum-controlled nuclear systems.

Acknowledgements

We thank Zong-Chao Yan for comments on the manuscript. This work was supported by the Strategic Priority Research Program of the Chinese Academy of Sciences (Grant Nos. XDB0920100 and XDB0920101), the National

Natural Science Foundation of China (Grant Nos. 12174402, 12393821, and 12274417), and the Chinese Academy of Sciences Project for Young Scientists in Basic Research (Grant No. YSBR-055).

References

[1] Brewer S M, Chen J S, Hankin A M, Clements E R, Chou C W, Wineland D J, Hume D B and Leibrandt D R 2019 *Phys. Rev. Lett.* **123** 033201

[2] Aeppli A, Kim K, Warfield W, Safronova M S and Ye J 2024 *Phys. Rev. Lett.* **133** 023401

[3] Marshall M C, Castillo D A R, Arthur-Dworschack W J, Aeppli A, Kim K, Lee D, Warfield W, Hinrichs J, Nardelli N V, Fortier T M, Ye J, Leibrandt D R and Hume D B 2025 *Phys. Rev. Lett.* **135** 033201

[4] Ludlow A D, Boyd M M, Ye J, Peik E and Schmidt P O 2015 *Rev. Mod. Phys.* **87** 637

[5] Gozzard D R, Howard L A, Dix-Matthews B P, Karpathakis S F E, Gravestock C T and Schediwy S W 2022 *Phys. Rev. Lett.* **128** 020801

[6] Dimarcq N, Gertsvolf M, Mileti G, *et al*. 2024 *Metrologia* **61** 012001

[7] Riehle F 2015 *Comptes Rendus. Physique* **16** 506

[8] Lodewyck J 2019 *Metrologia* **56** 055009

[9] Safronova M S, Budker D, DeMille D, Kimball D F J, Derevianko A and Clark C W 2018 *Rev. Mod. Phys.* **90** 025008

[10] Godun R M, Nisbet-Jones P B R, Jones J M, King S A, Johnson L A M, Margolis H S, Szymaniec K, Lea S N, Bongs K and Gill P 2014 *Phys. Rev. Lett.* **113** 210801

[11] Rosenband T, Hume D B, Schmidt P O, Chou C W, Brusch A, Lorini L, Oskay W H, Drullinger R E, Fortier T M, Stalnaker J E, Diddams S A, Swann W C, Newbury N R, Itano W M, Wineland D J and Bergquist J C 2008 *Science* **319** 1808

[12] Fuchs E, Kirk F, Madge E, Paranjape C, Peik E, Perez G, Ratzinger W and Tiedau J 2025 *Phys. Rev. X* **15** 021055

[13] Filzinger M, Dörscher S, Lange R, Klose J, Steinel M, Benkler E, Peik E, Lisdat C and Huntemann N 2023 *Phys. Rev. Lett.* **130** 253001

[14] Boulder Atomic Clock Optical Network BACON Collaboration 2021 *Nature* **591** 564

[15] Derevianko A and Pospelov M 2014 *Nat. Phys.* **10** 933

[16] Wcisło P, Ablewski P, Beloy K, *et al*. 2018 *Sci. Adv.* **4** eaau4869

[17] Xu G (ed) 2013 *Sciences of Geodesy - II: Innovations and Future Developments* (Berlin, Heidelberg: Springer Berlin Heidelberg)

[18] Zhao G, Xia J, Liu Y, *et al*. 2025 *Chin. Phys. Lett.* **42** 063701

[19] Deng S, Ren W, Xiang J, Zhao J, Li L, Zhang D, Wan J, Meng Y, Jiang X, Li T, Liu L and Lü D 2024 *Chin. Phys. B* **33** 070602

[20] Kaplan E D and Hegarty C (eds) 2006 *Understanding GPS : Principles and Applications* (Boston: Artech House)

[21] Jin S (ed) 2012 *Global Navigation Satellite Systems: Signal, Theory and Applications* (Rijeka: IntechOpen)

[22] Campbell C J, Radnaev A G, Kuzmich A, Dzuba V A, Flambaum V V and Derevianko A 2012 *Phys. Rev. Lett.* **108** 120802

[23] Beloy K 2023 *Phys. Rev. Lett.* **130** 103201

[24] Peik E and Tamm C 2003 *Europhys. Lett.* **61** 181

[25] Dzuba V A and Flambaum V V 2023 *Phys. Rev. A* **108** 062813

[26] Tiedau J, Okhapkin M V, Zhang K, Thielking J, Zitzer G, Peik E, Schaden F, Pronebner T, Morawetz I, De Col L T, Schneider F, Leitner A, Pressler M, Kazakov G A, Beeks K, Sikorsky T and Schumm T 2024 *Phys. Rev. Lett.* **132** 182501

[27] Elwell R, Schneider C, Jeet J, Terhune J E S, Morgan H W T, Alexandrova A N, Tran Tan H B, Derevianko A and Hudson E R 2024 *Phys. Rev. Lett.* **133** 013201

[28] Zhang C, Ooi T, Higgins J S, Doyle J F, von der Wense L, Beeks K, Leitner A, Kazakov G A, Li P, Thirol P G, Schumm T and Ye J 2024 *Nature* **633** 63

[29] Higgins J S, Ooi T, Doyle J F, Zhang C, Ye J, Beeks K, Sikorsky T and Schumm T 2025 *Phys. Rev. Lett.* **134** 113801

[30] Das S, Pálffy A and Keitel C H 2013 *Phys. Rev. C* **88** 024601

[31] Li L, Li Z, Wang C, Gan W T, Hua X and Tong X 2023 *Nuc. Sci. Tech.* **34** 1698

[32] Campbell C J, Steele A V, Churchill L R, DePalatis M V, Naylor D E, Matsukevich D N, Kuzmich A and Chapman M S 2009 *Phys. Rev. Lett.* **102** 233004

[33] Rellergert W G, DeMille D, Greco R R, Hehlen M P, Torgerson J R and Hudson E R 2010 *Phys. Rev. Lett.* **104** 200802

[34] Kazakov G A, Litvinov A N, Romanenko V I, Yatsenko L P, Romanenko A V, Schreitl M, Winkler G and Schumm T 2012 *New J. Phys.* **14** 083019

[35] Beeks K, Sikorsky T, Schumm T, Thielking J, Okhapkin M V and Peik E 2021 *Nat. Rev. Phys.* **3** 238

[36] Von Der Wense L and Seiferle B 2020 *Eur. Phys. J. A* **56** 176

[37] Groot-Berning K, Stopp F, Jacob G, Budker D, Haas R, Renisch D, Runke J, Thörle-Pospiech P, Düllmann C E and Schmidt-Kaler F 2019 *Phys. Rev. A* **99** 023420

[38] Flambaum V V 2006 *Phys. Rev. Lett.* **97** 092502

[39] Kolkowitz S, Pikovski I, Langellier N, Lukin M D, Walsworth R L and Ye J 2016 *Phys. Rev. D* **94** 124043

[40] Porsev S G, Flambaum V V, Peik E and Tamm Chr 2010 *Phys. Rev. Lett.* **105** 182501

[41] Porsev S G and Flambaum V V 2010 *Phys. Rev. A* **81** 042516

[42] Bilous P V, Peik E and Palffy A 2018 *New J. Phys.* **20** 013016

[43] Porsev S G, Cheung C and Safronova M S 2021 *Quantum Sci. Technol.* **6** 034014

[44] Leander G and Sheline R 1984 *Nuclear Physics A* **413** 375

[45] Gulda K, Kurcewicz W, Aas A, Borge M, Burke D, Fogelberg B, Grant I, Hagebø E, Kaffrell N, Kvasil J, *et al*. 2002 *Nuclear Physics A* **703** 45

[46] Flambaum V V and Wiringa R B 2009 *Phys. Rev. C* **79** 034302

[47] Moore K T and van der Laan G 2009 *Rev. Mod. Phys.* **81** 235

[48] Okhapkin M V, Meier D M, Peik E, Safronova M S, Kozlov M G and Porsev S G 2015 *Phys. Rev. A* **92** 020503

[49] Minkov N and Pálffy A 2017 *Phys. Rev. Lett.* **118** 212501

[50] Zhang H and Wang X 2023 *Front. Phys.* **11** 1166566

[51] Kozioł K and Rzadkiewicz J 2025 *Phys. Rev. C* **111** 064302

[52] Herrera-Sancho O A, Nemitz N, Okhapkin M V and Peik E 2013 *Phys. Rev. A* **88** 012512

[53] Kroger L A and Reich C W 1976 *Nuclear Physics A* **259** 29

[54] Reich C W and Helmer R G 1990 *Phys. Rev. Lett.* **64** 271

[55] Helmer R G and Reich C W 1994 *Phys. Rev. C* **49** 1845

[56] Beck B R, Becker J A, Beiersdorfer P, Brown G V, Moody K J, Wilhelmy J B, Porter F S, Kilbourne C A and Kelley R L 2007 *Phys. Rev. Lett.* **98** 142501

[57] Beck B, Wu C, Beiersdorfer P, Brown G, Becker J, Moody K, Wilhelmy J, Porter F, Kilbourne C and Kelley R 2009 *Proc. 12th International Conference on Nuclear Reaction Mechanisms LLNL-PROC-415170* (Varenna, Italy)

[58] Seiferle B, Von Der Wense L, Bilous P V, Amersdorffer I, Lemell C, Libisch F, Stellmer S, Schumm T, Düllmann C E, Pálffy A and Thirolf P G 2019 *Nature* **573** 243

[59] Kraemer S, Moens J, Athanasakis-Kaklamanakis M, *et al*. 2023 *Nature* **617** 706

[60] Yamaguchi A, Muramatsu H, Hayashi T, Yuasa N, Nakamura K, Takimoto M, Haba H, Konashi K, Watanabe M, Kikunaga H, Maehata K, Yamasaki N Y and Mitsuda K 2019 *Phys. Rev. Lett.* **123** 222501

[61] Sikorsky T, Geist J, Hengstler D, Kempf S, Gastaldo L, Enss C, Mokry C, Runke J, Düllmann C E, Wobrauschek P, Beeks K, Rosecker V, Sterba J H, Kazakov G, Schumm T and Fleischmann A 2020 *Phys. Rev. Lett.* **125** 142503

[62] Hiraki T, Okai K, Bartokos M, *et al*. 2024 *Nat. Commun.* **15** 5536

[63] Zhang C, Von Der Wense L, Doyle J F, Higgins J S, Ooi T, Friebel H U, Ye J, Elwell R, Terhune J E S, Morgan H W T, Alexandrova A N, Tran Tan H B, Derevianko A and Hudson E R 2024 *Nature* **636** 603

[64] Elwell R, Terhune J E S, Schneider C, Morgan H W T, Tan H B T, Perera U C, Rehn D A, Alfonso M C, von der Wense L, Seiferle B, Scharl K, Thirolf P G, Derevianko A and Hudson E R 2025 *Nature* **648** 300

[65] Yamaguchi A, Shigekawa Y, Haba H, Kikunaga H, Shirasaki K, Wada M and Katori H 2024 *Nature* **629** 62

[66] Schwartz C 1955 *Phys. Rev.* **97** 380

[67] Wang W and Wang X 2024 *Phys. Rev. Lett.* **133** 032501

[68] Müller R A, Maiorova A V, Fritzsche S, Volotka A V, Beerwerth R, Glowacki P, Thielking J, Meier D M, Okhapkin M, Peik E and Surzhykov A 2018 *Phys. Rev. A* **98** 020503

[69] Li F C, Qiao H X, Tang Y B and Shi T Y 2021 *Phys. Rev. A* **104** 062808
[70] Minkov N and Pálffy A 2019 *Phys. Rev. Lett.* **122** 162502
[71] Campbell C J, Radnaev A G and Kuzmich A 2011 *Phys. Rev. Lett.* **106** 223001
[72] Zitzer G, Tiedau J, Düllmann C E, Okhapkin M V and Peik E 2025 *Phys. Rev. A* **111** L050802
[73] Thielking J, Okhapkin M V, Glowacki P, Meier D M, von der Wense L, Seiferle B, Duellmann C E, Thirolf P G and Peik E 2018 *Nature* **556** 321
[74] Fadeev P, Berengut J C and Flambaum V V 2020 *Phys. Rev. A* **102** 052833
[75] Safronova M S, Safronova U I, Radnaev A G, Campbell C J and Kuzmich A 2013 *Phys. Rev. A* **88** 060501
[76] Chasman R R, Ahmad I, Friedman A M and Erskine J R 1977 *Rev. Mod. Phys.* **49** 833
[77] Berengut J C, Dzuba V A, Flambaum V V and Porsev S G 2009 *Phys. Rev. Lett.* **102** 210801
[78] Bemis C E, McGowan F K, Jr J L C F, Milner W T, Robinson R L, Stelson P H, Leander G A and Reich C W 1988 *Phys. Scr.* **38** 657
[79] Safronova M S and Safronova U I 2013 *Phys. Rev. A* **87** 062509
[80] Dzuba V A and Flambaum V V 2023 *Phys. Rev. Lett.* **131** 263002
[81] Thirolf P G, Kraemer S, Moritz D and Scharl K 2024 *Eur. Phys. J. Spec. Top.* **233** 1113
[82] Peik E, Schumm T, Safronova M S, Palffy A, Weitenberg J and Thirolf P G 2021 *Quantum Sci. Technol.* **6** 034002
[83] Roberts B M, Dzuba V A and Flambaum V V 2013 *Phys. Rev. A* **88** 012510
[84] Safronova M S, Safronova U I and Clark C W 2014 *Phys. Rev. A* **90** 032512
[85] Keele J A, Lundeen S R and Fehrenbach C W 2011 *Phys. Rev. A* **83** 062509
[86] Bruneau J 1983 *J. Phys. B: At. Mol. Phys.* **16** 4135
[87] Denis-Petit D, Gosselin G, Hannachi F, Tarisien M, Bonnet T, Comet M, Gobet F, Versteegen M, Morel P, Méot V and Matea I 2017 *Phys. Rev. C* **96** 024604
[88] Desclaux J P 1989 *AIP Conference Proceedings* **189** 265
[89] Desclaux J 1975 *Computer Physics Communications* **9** 31
[90] Zubova N A, Anisimova I S, Kaygorodov M Y, Kozhedub Y S, Malyshev A V, Shabaev V M, Tupitsyn I I, Plunien G, Brandau C and Stöhlker T 2019 *J. Phys. B: At. Mol. Phys.* **52** 185001
[91] Si R, Shi C, Xue N, Kong X, Chen C, Tu B and Ma Y G 2025 *Sci. China Phys. Mech. Astron.* **68** 272011
[92] Kitovienė L, Gaigalas G, Rynkun P, Domoto N, Tanaka M and Kato D 2025 *Mon. Not. R. Astron. Soc.* **538** 92
[93] Dzuba V A 2005 *Phys. Rev. A* **71** 062501
[94] Dzuba V A, Flambaum V V and Kozlov M G 1996 *Phys. Rev. A* **54** 3948
[95] Safronova U I, Johnson W R and Safronova M S 2007 *Phys. Rev. A* **76** 042504
[96] Savukov I M 2020 *Atoms* **8** 87
[97] Yu S C, Gan W T, Hua X, Tong X and Li C B 2024 *Phys. Rev. A* **109** 063115
[98] Blundell S A, Johnson W R and Sapirstein J 1991 *Phys. Rev. A* **43** 3407
[99] Li F C, Tang Y B, Qiao H X and Shi T Y 2021 *J. Phys. B: At. Mol. Phys.* **54** 145004
[100] Li F, Ma H and Tang Y B 2021 *J. Phys. B: At. Mol. Phys.* **54** 065003
[101] Safronova U I, Johnson W R and Safronova M S 2006 *Phys. Rev. A* **74** 042511
[102] Tang Y B, Gao N N, Lou B Q and Shi T Y 2018 *Phys. Rev. A* **98** 062511
[103] Safronova M S, Safronova U I and Kozlov M G 2018 *Phys. Rev. A* **97** 012511
[104] Safronova M S, Porsev S G, Kozlov M G, Thielking J, Okhapkin M V, Głowacki P, Meier D M and Peik E 2018 *Phys. Rev. Lett.* **121** 213001
[105] Gamrath S, Godefroid M R, Palmeri P, Quinet P and Wang K 2020 *Monthly Notices of the Royal Astronomical Society* **496** 4507
[106] Flambaum V V, Dzuba V A and Peik E 2025 *Phys. Rev. A* **112** 023103
[107] Mazzone G, Michelini M D C, Russo N and Sicilia E 2008 *Inorg. Chem.* **47** 2083
[108] Biémont E, Fivet V and Quinet P 2004 *J. Phys. B: Atom. Mol. Opt. Phys.* **37** 4193
[109] Migdalek J and Glowacz-Proszkiewicz A 2007 *J. Phys. B* **40** 4143
[110] Gossel G H, Dzuba V A and Flambaum V V 2013 *Phys. Rev. A* **88** 034501
[111] Safronova U I, Safronova M S and Johnson W R 2017 *Phys. Rev. A* **95** 042507
[112] Li F C, Qiao H X, Tang Y B and Shi T Y 2022 *J. Quant. Spectrosc. Radiat. Transf.* **288** 108241
[113] Eliav E and Kaldor U 2012 *Chem. Phys.* **392** 78
[114] S Fraga J K and Saxena K Elsevier, Amsterdam, 1976 *Handbook of Atomic Data* (Amsterdam: Elsevier)
[115] Lim I S and Schwerdtfeger P 2004 *Phys. Rev. A* **70** 062501
[116] Safronova U I and Safronova M S 2011 *Phys. Rev. A* **84** 052515
[117] Tkalya E V and Nikolaev A V 2016 *Phys. Rev. C* **94** 014323
[118] Yerokhin V A and Surzhykov A 2019 *J. Phys. Chem. Ref. Data* **48** 033104
[119] Kramida A, Ralchenko Y, Reader J and NIST ASD Team *NIST Atomic Spectra Database*
[120] Porsev S G and Flambaum V V 2010 *Phys. Rev. A* **81** 032504
[121] Karpeshin F F, Wycech S, Band I M, Trzhaskovskaya M B, Pfützner M and Żylicz J 1998 *Phys. Rev. C* **57** 3085
[122] Paris-Saclay U 2023 *Lac database*
[123] Dzuba V A and Flambaum V V 2016 *Phys. Rev. A* **93** 052517
[124] Torbohm G, Fricke B and Rosén A 1985 *Phys. Rev. A* **31** 2038
[125] Perera U C, Morgan H W T, Hudson E R and Derevianko A 2025 *Phys. Rev. Lett.***135** 123001
[126] Itano W M 2000 *J. Res. Natl. Inst. Stand. Technol.* **105** 829
[127] Gan H C J, Maslennikov G, Tseng K W, Tan T R, Kaewuam R, Arnold K J, Matsukevich D and Barrett M D 2018 *Phys. Rev. A* **98** 032514
[128] Rellergert W G, Sullivan S T, DeMille D, Greco R R, Hehlen M P, Jackson R A, Torgerson J R and Hudson E R 2010 *IOP Conf. Ser. Mater. Sci. Eng.* **15** 012005
[129] Stellmer S, Kazakov G, Schreitl M, Kaser H, Kolbe M and Schumm T 2018 *Phys. Rev. A* **97** 062506
[130] Morgan H W T, Tan H B T, Elwell R, Alexandrova A N, Hudson E R and Derevianko A 2025 *Phys. Rev. Lett.* **134** 253801
[131] Terhune J E S, Elwell R, Tan H B T, Perera U C, Morgan H W T, Alexandrova A N, Derevianko A and Hudson E R 2025 *Phys. Rev. Res.* **7** L022062
[132] Dessovic P, Mohn P, Jackson R A, Winkler G, Schreitl M, Kazakov G and Schumm T 2014 *J. Phys. Condens. Matter* **26** 105402
[133] Dubé P, Madej A A, Bernard J E, Marmet L, Boulanger J S and Cundy S 2005 *Phys. Rev. Lett.* **95** 033001
[134] Huang Y, Zhang B, Zeng M, Hao Y, Ma Z, Zhang H, Guan H, Chen Z, Wang M and Gao K 2022 *Phys. Rev. Appl.* **17** 034041
[135] Chiara C J, Carroll J J, Carpenter M P, Greene J P, Hartley D J, Janssens R V F, Lane G J, Marsh J C, Matters D A, Polasik M, Rzadkiewicz J, Seweryniak D, Zhu S, Bottoni S, Hayes A B and Karamian S A 2018 *Nature* **554** 216
[136] Wu Y, Gunst J, Keitel C H and Pálffy A 2018 *Phys. Rev. Lett.* **120** 052504
[137] Qi J, Zhang H and Wang X 2023 *Phys. Rev. Lett.* **130** 112501
[138] Wang W, Zhou J, Liu B and Wang X 2021 *Phys. Rev. Lett.* **127** 052501
[139] Wang X 2022 *Phys. Rev. C* **106** 024606
[140] Wang W and Wang X 2023 *Phys. Rev. Res.* **5** 043232
[141] Bilous P V, Minkov N and Pálffy A 2018 *Phys. Rev. C* **97** 044320
[142] Meier D M, Thielking J, Głowacki P, Okhapkin M V, Müller R A, Surzhykov A and Peik E 2019 *Phys. Rev. A* **99** 052514
[143] Wang W, Zou F, Fritzsche S and Li Y 2024 *Phys. Rev. Lett.***133** 223001
[144] Dzuba V A and Flambaum V V 2025 *Phys. Rev. A* **111** 053109
[145] Dzuba V A and Flambaum V V 2025 *Phys. Rev. A* **111** L041103
[146] Müller R A, Volotka A V and Surzhykov A 2019 *Phys. Rev. A* **99** 042517
[147] Bilous P V, Bekker H, Berengut J C, Seiferle B, von der Wense L, Thirolf P G, Pfeifer T, López-Urrutia J R C and Pálffy A 2020 *Phys. Rev. Lett.* **124** 192502
[148] Wang W, Fritzsche S and Li Y 2025 *Phys. Rev. A* **112** 022811